ornl

ORNL/TM-10988

OAK RIDGE
NATIONAL
LABORATORY

MARTIN MARIETTA

# Runaway Studies in the ATF Torsatron


A. C. England
G. L. Bell
W. R. DeVan
C. C. Eberle
R. H. Fowler
W. A. Gabbard
J. C. Glowienka
J. H. Harris
G. R. Haste
R. R. Kindsfather
R. N. Morris
M. Murakami
G. H. Neilson
D. A. Rasmussen
J. A. Rome
M. J. Saltmarsh
J. B. Wilgen
W. R. Wing
K. G. Young





OPERATED BY
MARTIN MARIETTA ENERGY SYSTEMS, INC.
FOR THE UNITED STATES
DEPARTMENT OF ENERGY

Printed in the United States of America. Available from
National Technical Information Service
U.S. Department of Commerce
5285 Port Royal Road, Springfield, Virginia 22161
NTIS price codes—Printed Copy: A04; Microfiche A01

ORNL/TM-10988
Dist. Category UC-420

Fusion Energy Division

# RUNAWAY STUDIES IN THE ATF TORSATRON

A. C. England
W. R. DeVan
C. C. Eberle
R. H. Fowler
W. A. Gabbard
J. C. Glowienka
J. H. Harris
G. R. Haste
R. R. Kindsfather
R. N. Morris
M. Murakami
G. H. Neilson
D. A. Rasmussen
J. A. Rome
M. J. Saltmarsh
J. B. Wilgen
W. R. Wing
K. G. Young

G. L. Bell
Auburn University

Date Published - January 1989

Prepared by the
OAK RIDGE NATIONAL LABORATORY
Oak Ridge, Tennessee 37831
operated by
MARTIN MARIETTA ENERGY SYSTEMS, INC.
for the
U.S. DEPARTMENT OF ENERGY
under contract DE-AC05-84OR21400

## CONTENTS

## ABSTRACT

Pulsed torsatrons and heliotrons are susceptible to runaway electron formation and confinement resulting from the inherent good containment in the vacuum fields and the high loop voltages during the initiation and termination of the helical and vertical fields ("field ramping"). Because runaway electrons can cause an unacceptable level of hard X rays near the machine, a runaway suppression system was designed and included in the initial operation of the Advanced Toroidal Facility (ATF). The main component of the system is a rotating paddle that is normally left in the vacuum chamber during the field ramps. This device proved to be very effective in reducing the runaway population. Measurements of hard X rays from ATF have shown that the runaways are produced primarily during the field ramping but that usually a small steady-state runaway component is also present during the "flat-top" portion of the fields. The paddle is the main source of the hard X rays (thick-target bremsstrahlung), although other objects in the vacuum chamber also serve as targets for the runaways at various times. The maximum X-ray energy found by pulse height analysis is ~12–15 MeV; the mean energy appears to be a few mega-electron-volts. A noticeable forward peaking of the bremsstrahlung from the paddle is evident. The limiters do not appear to be major sources of bremsstrahlung.

# 1. INTRODUCTION

Pulsed torsatrons and heliotrons are susceptible to the production of runaway electrons and the concomitant hard X-ray production where the runaways strike the vacuum vessel and internal structures. The runaways are accelerated by the relatively high loop voltages produced by the ramp-up and ramp-down of the fields and are contained in the vessel by virtue of the good flux surfaces from the moment of creation of the magnetic fields. The high loop voltages produced during ramp-down often produce the more serious problem because plasma in the vessel can provide free electrons to be accelerated by the loop voltage. Although a steady-state device should have no such problems during the steady-state phase, precautions might still have to be taken during rapid ramping of the fields to avoid high X-ray doses and damage to the internal structure or walls of the device.

We report here on the runaways associated with operation of the Advanced Toroidal Facility (ATF). ATF is a torsatron with a major radius of 2.1 m and an average minor radius of 0.27 m. It is an $\ell = 2$, 12-field-period ($m = 12$) device with a maximum magnetic field of 2 T. The rotational transform, $\epsilon$, varies between $\sim$0.3 (axis) and $\sim$1.0 (wall) for the standard magnetic configuration. The magnetic fields are produced by two helical field (HF) coils and three sets of poloidal field coils (designated the inner, mid, and outer vertical field coils). The outer vertical field coil set has two separate electrical systems: a main outer vertical field in series with the helical field and a trim field used for plasma position control. The inner vertical field is used for position control and shaping. The mid vertical field coil is designed primarily for plasma shaping and was not used during the period discussed in this paper. The operation reported here involves fields only up to $\sim$1 T. Plasma is produced by a 200-kW gyrotron at 53.2 GHz, utilizing electron cyclotron heating (ECH) at the second harmonic. Plasma heating has also used neutral beam injection from two beam lines ultimately capable of $\sim$2 MW at $\sim$40 keV. A complete description of the device, the design, and construction has been given by J. F. Lyon et al.[1] The initial plasma operation has been described by G. H. Neilson et al.[2] Operation with neutral beam injection has been discussed by M. J. Saltmarsh et al.[3]

## 2. EXPERIENCE FROM HELIOTRON-E AND OTHER STELLARATORS

During the initial phases of operation of Heliotron-E, photoneutrons were observed and found to be the result of high-energy runaway electrons.[4] The bremsstrahlung energy spectra showed hard X rays with energies greater than 10 MeV. Radioactivity was found in the limiters and vacuum chamber, which could be attributed to the runaway electrons causing a variety of photonuclear reactions. In late 1986, during a series of experiments with no auxiliary vertical field (AVF), a serious runaway problem was found on Heliotron-E.[5] Normally, the drift surfaces are shifted outward during HF ramp-up and ramp-down to force runaways to scrape off on the walls and limiters during the acceleration period. With the AVF disabled, this was not possible, and large X-ray doses were observed inside the Heliotron-E machine room.

Our calculations, given in Fig. 1, show the effect of the AVF on the flux surfaces in Heliotron-E at a toroidal angle of 0° ($\Phi = 0°$). Figure 1(a) is a Poincaré plot of the magnetic flux surfaces for the normal AVF ($I_{\mathrm{AVF}}/I_{\mathrm{HF}} = 0.121$), and Fig. 1(b) is a Poincaré plot of the flux surfaces for an AVF of twice this value ($I_{\mathrm{AVF}}/I_{\mathrm{HF}} = 0.242$). Although flux surfaces are still seen in Fig. 1(b), the quality of the surfaces is much poorer and they occupy a much smaller fraction of the available volume.

Our calculations showed that horizontal error fields should have little effect on the drift surfaces. Figure 2 shows Poincaré plots at $\Phi = 0°$ for shifted-out [Fig. 2(a)] and shifted-out and perturbed [Fig. 2(b)] cases where the perturbation was an $\sim$4-g horizontal error field. It is clear that the flux surfaces are still quite good in the latter case.

On Heliotron-E, an inward shift was also tried, and the effect was to make the runaway problem much worse.[5] The inward shift moves the runaway electron orbits away from the walls and limiters and permits better containment. Normally, the shift of the electron orbit from the flux surface is inward during ramp-up and outward during ramp-down. By shifting the drift surfaces outward intentionally during ramp-up, the normal inward shift is canceled and the orbits intercept the walls and limiters. An inward shift during ramp-up increases the containment volume and allows a longer acceleration period. Later, when the runaways are lost and strike the vacuum chamber, the X-ray intensity can be much higher.

Runaways have been observed in stellarators for at least three decades.[6–9] Correlations between magnetic fluctuations and runaways were observed in Uragan-2

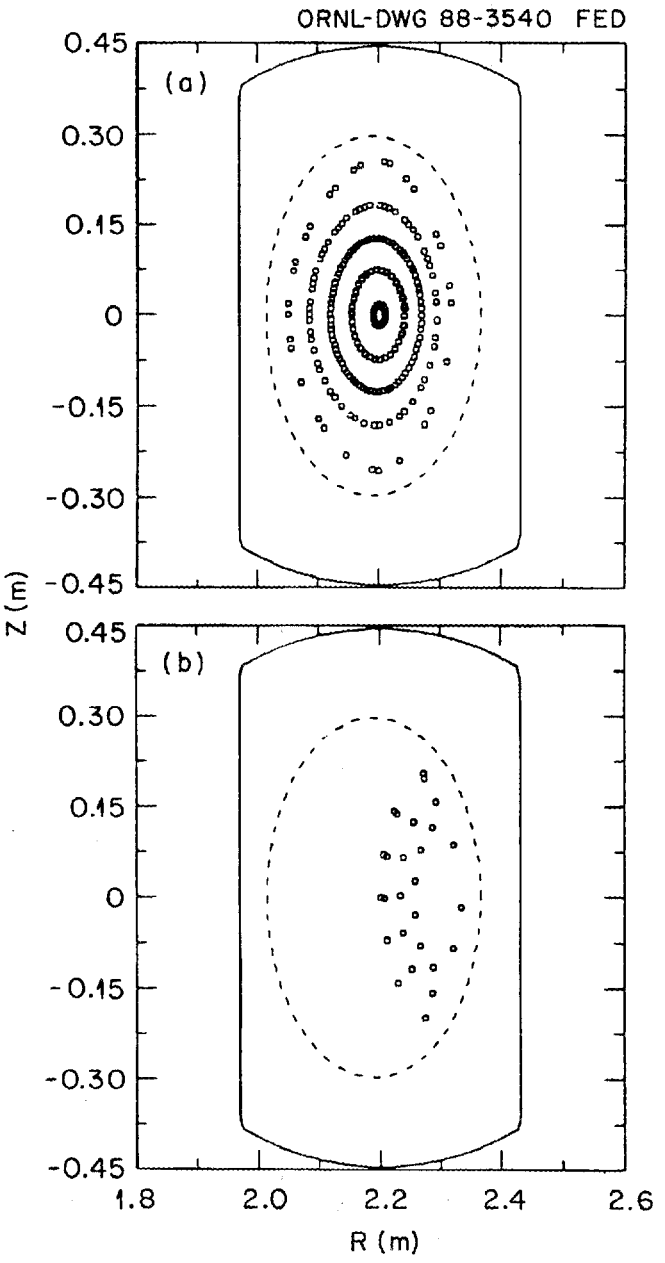


Fig. 1. Poincaré plots of the magnetic surfaces in Heliotron-E: (a) normal auxiliary vertical field, $I_{\mathrm{AVF}}/I_{\mathrm{HF}} = 0.121$, and (b) shifted-out configuration with twice the normal auxiliary field, $I_{\mathrm{AVF}}/I_{\mathrm{HF}} = 0.242$.

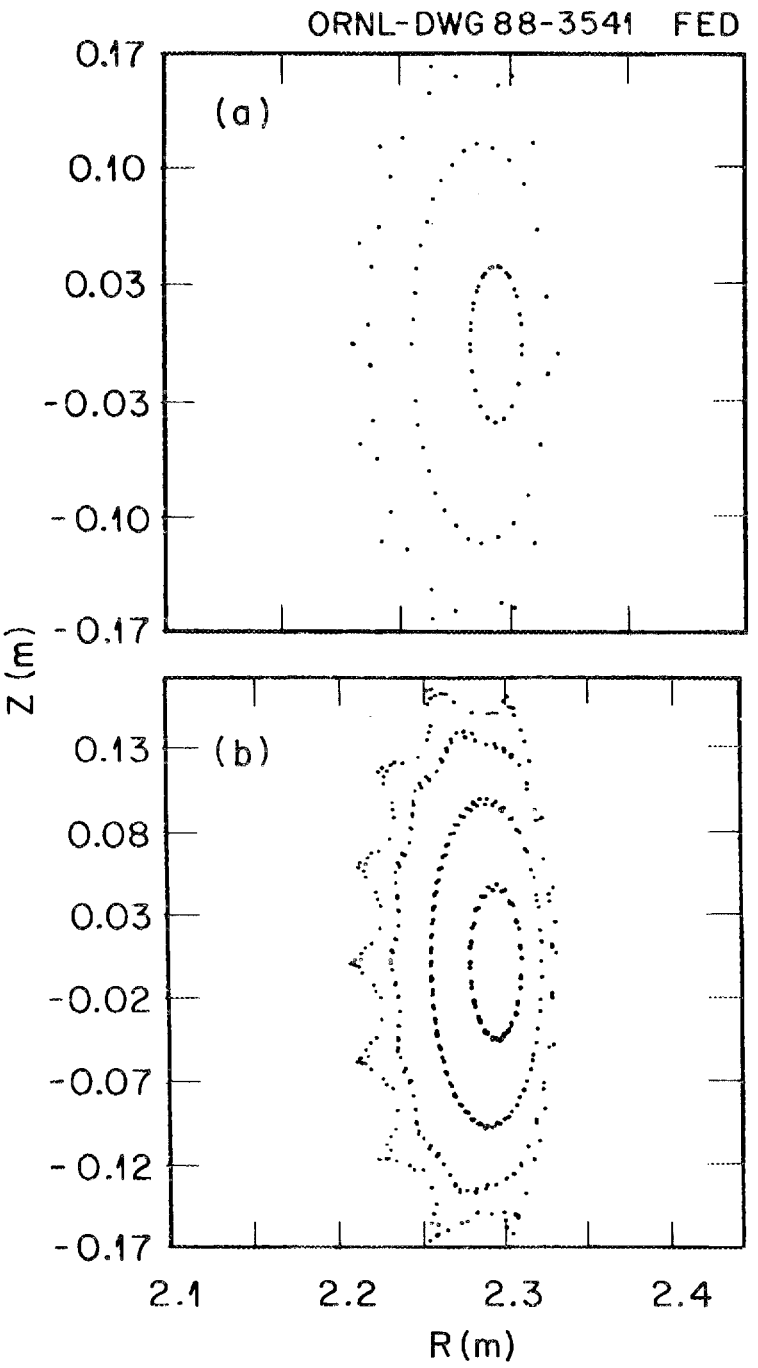


Fig. 2. Poincaré plots of the magnetic surfaces in Heliotron-E: (a) shifted-out configuration with no horizontal error field and (b) shifted-out configuration with a 4-g horizontal error field.

with ohmic heating.[10] Runaway electrons with energies up to 4–5 MeV were observed from that device. Runaway electrons were also observed in Proto-Cleo[11] when it was operated as a torsatron. In Torso,[12] where the magnetic configuration was invariant, runaways up to ~2 MeV were observed at low density.

## 3. DRIFT SURFACES AND RUNAWAY ORBIT CALCULATIONS FOR ATF

Poincaré plots for ATF with normal flux surfaces using a standard vertical field configuration are shown in Fig. 3(a) at the toroidal angle cut through the center of the vertical port ($\Phi = 0$). Similarly, Poincaré plots for the shifted-out flux surfaces using only the main vertical field coils (in series with the helical field) are shown in Fig. 3(b). It is clear in the latter case that good flux surfaces still exist in ATF with the maximum achievable outward shift. Using the maximum of the trim and inner vertical fields will move the flux surfaces far inward but still not eliminate good surfaces. Calculations show that using one of the mid vertical field coils (top or bottom only) would shift the flux surfaces down or up but would also not destroy the good flux surfaces.

Relativistic electron orbits have also been studied in the ATF geometry. Figure 4 shows the guiding center orbit of a typical 5-MeV electron projected onto a $\Phi$ = constant plane in the standard ATF field. The loops in the orbit are the result of twisting of the flux surfaces. The particle cannot be followed reliably for long time periods because of the accumulation of numerical errors. However, it appears that a wide class of particles is well contained. The particles appear to be confined up and down symmetrically in the vicinity of the midplane.

Figure 5(a) shows a Poincaré plot of relativistic electron orbits for a number of energies (0.6 to 50 MeV) during ramp-up of the fields. The orbits at higher energies are shifted inward more than those at the lower energies. The shift of orbits with electrons going in the same direction as the field (co-orbits) is inward. Similarly, Fig. 5(b) shows the electron orbit Poincaré plot for the ramp-down, indicating the outward shift for the high-energy electrons. In this case the electrons are accelerated in the direction opposite to the field by the reversed loop voltage. Near 50 MeV, the orbit becomes very small because the vertical drifts ($\sim v^2$) cancel the poloidal component of $v_{\|}$. All of the particles in Fig. 5(a) are started at $Z = 0$ m and $R = 1.91$ m, while all of the particles in Fig. 5(b) are started at $Z = 0$ m and

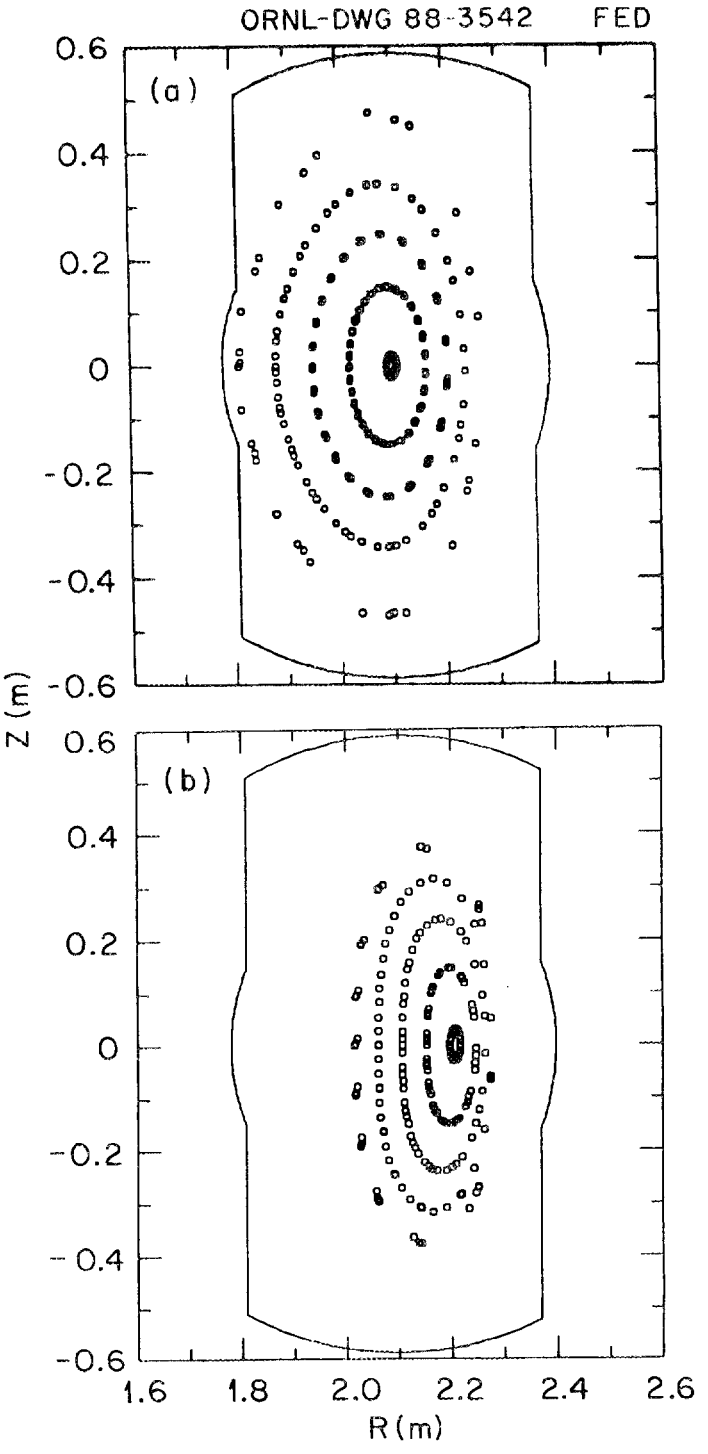


Fig. 3. Poincaré plots of the magnetic surfaces in ATF: (a) standard configuration using the trim vertical field, and (b) trim vertical field = 0.

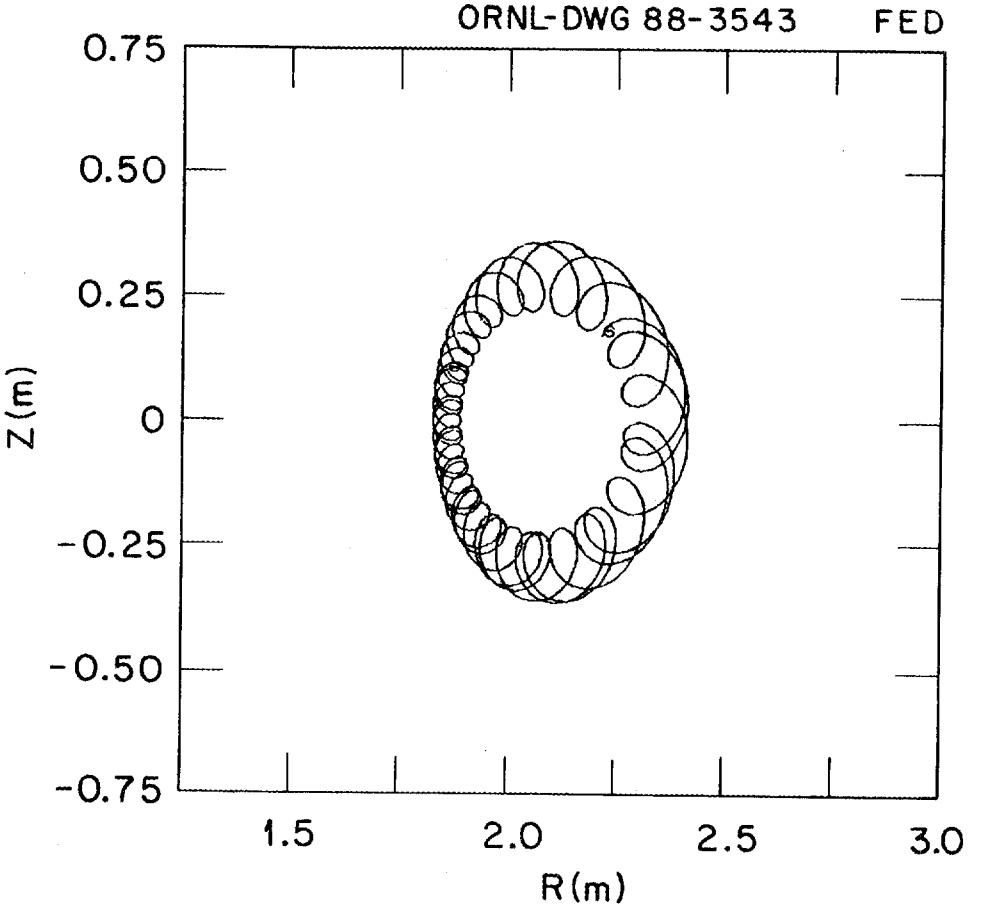


Fig. 4. Orbit of a typical 5-MeV electron projected onto a $\Phi$ = constant plane for a standard ATF field.

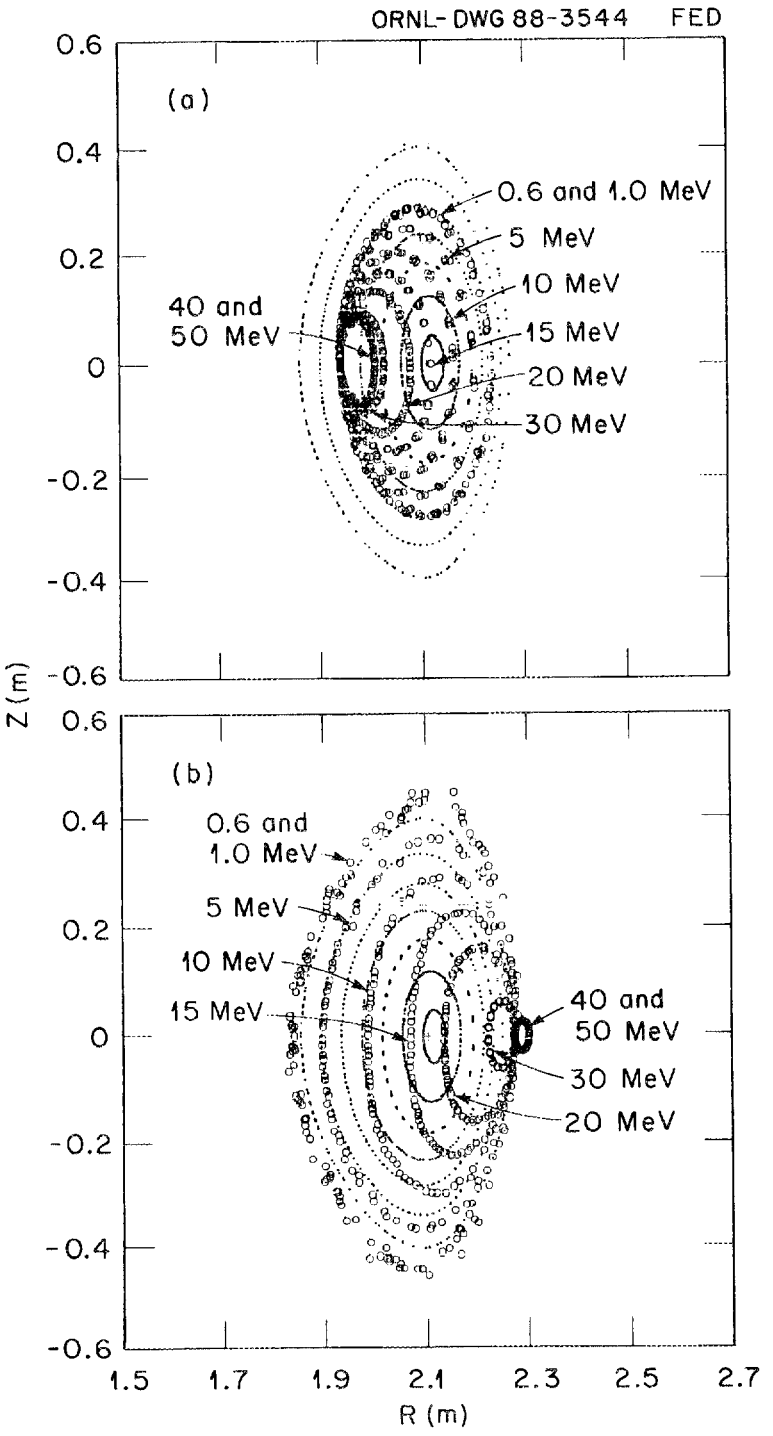


Fig. 5. Poincaré plots of relativistic electron orbits for a number of energies between 0.6 and 50 MeV in ATF superimposed on a set of magnetic flux surfaces in the $\Phi = 0$ plane: (a) during ramp-up of the fields and (b) during ramp-down of the fields.

$R = 2.25$ m. The difference in orbit sizes between Figs. 5(a) and 5(b) is the result of different starting point locations.

# 4. HARD X-RAY SUPPRESSION TECHNIQUES AND DIAGNOSTICS ON ATF

## 4.1 TECHNIQUES

Because of the concerns about runaway production and the associated hazard to the device and personnel, a concerted effort was made to employ several techniques to reduce the hazards. Four techniques are used to aid in runaway suppression and control. The first of these is the technique employed on Heliotron-E: vertical field programming. This technique did not initially appear to be easily applicable to ATF because the arrangement of coils and power supplies on ATF does not allow the drift surfaces to be shifted out as far as in the case of Heliotron-E. To apply this technique to ATF, the helical fields are allowed to ramp up with no trim vertical field so that the drift surfaces remain shifted out as far as possible during the time when the loop voltage is present. Only near the end of the ramp is the trim field applied. This means that the trim field is normally delayed by ~200 ms from the helical field. This is discussed further in Sect. 5.1.

The second technique employs a rotating paddle, which normally remains in the center of the vacuum vessel and is removed (swung out) only to allow plasma production. The paddle, which is supported from the top port, is left near the center of the vacuum chamber between shots and during the ramp-up, after which it is withdrawn. It is reinserted before the field ramp-down. The paddle is made of 0.165-cm-thick stainless steel and consists of a 1.27-cm-diam rotating arm and a flat blade, which together intercept 3–4% of the drift surfaces. The blade extends 10.95 cm radially and 5.08 cm vertically with the inner edge approximately positioned on the axis. The paddle and blade are grounded to the vacuum vessel through a small resistor to avoid charging and arcing. The design objective was to intercept the electrons before they could make more than ~100 toroidal transits, thus limiting their maximum energy. Since the maximum loop voltage is ~20 V during field ramping, the maximum energy that they should be able to reach is ~2 keV; however, the actual energies observed were many mega-electron-volts. These measurements are discussed in Sect. 5.2. In practice, the position of the paddle in the vessel can be varied somewhat to intercept the maximum number of runaways. Details of this

effort are given in Sect. 5.1. The paddle is located in sector 20 of ATF. Figure 6, a plan view of ATF, shows the location of the paddle, detectors, and other details to be described later.

The third technique uses a device consisting of a fast gas valve and a high-pressure reservoir, which rapidly fills the torus with a noble gas (He, Ar, or Xe) to decelerate the runaways and suppress the bremsstrahlung emission. This gas "bomb" is designed to fill the torus in ~10 ms to a pressure of $\sim 10^{-2}$ torr in the event of an unanticipated worst-case fault condition such as an abort of the helical fields during or just after plasma production (which would cause a high loop voltage in the presence of a plasma). This device was designed, built, and tested but never used for two reasons: (1) the worst-case scenario in which an abort occurs during plasma production did not produce the estimated runaway current and the concomitant X-ray emission, and (2) there was concern that there would be serious damage to some of the diagnostics because of the rapid change in pressure. Experimental details of the worst-case scenario are described in Sect. 6. Details of the design, construction, and operation of the rotating paddle and the gas bomb are discussed by Rasmussen et al.[13]

The final technique applied is to minimize the loop voltage during the "flat-top" portion of the fields. This requires careful programming of the silicon-controlled rectifier (SCR) firings so that a minimum loop voltage is present during this time. It is not always possible to keep this voltage at zero because of the varying conditions imposed on the operation. The residual loop voltage is typically <0.1 V but occasionally can be considerably larger. Such a voltage can continually accelerate free electrons produced during the ramp-up or during the ECH plasma production period.

## 4.2 DIAGNOSTICS

The main diagnostics for the runaway studies consisted of the following:

1. Two NaI(Tl) scintillators mounted on phototubes with the phototubes operating in the current mode. These are chiefly used to give the time behavior of the hard X-ray intensity and are not calibrated.
2. Two ionization chambers. These are calibrated to give the dose rate at the location of the chamber, but they are fairly slow with response times of a few milliseconds.

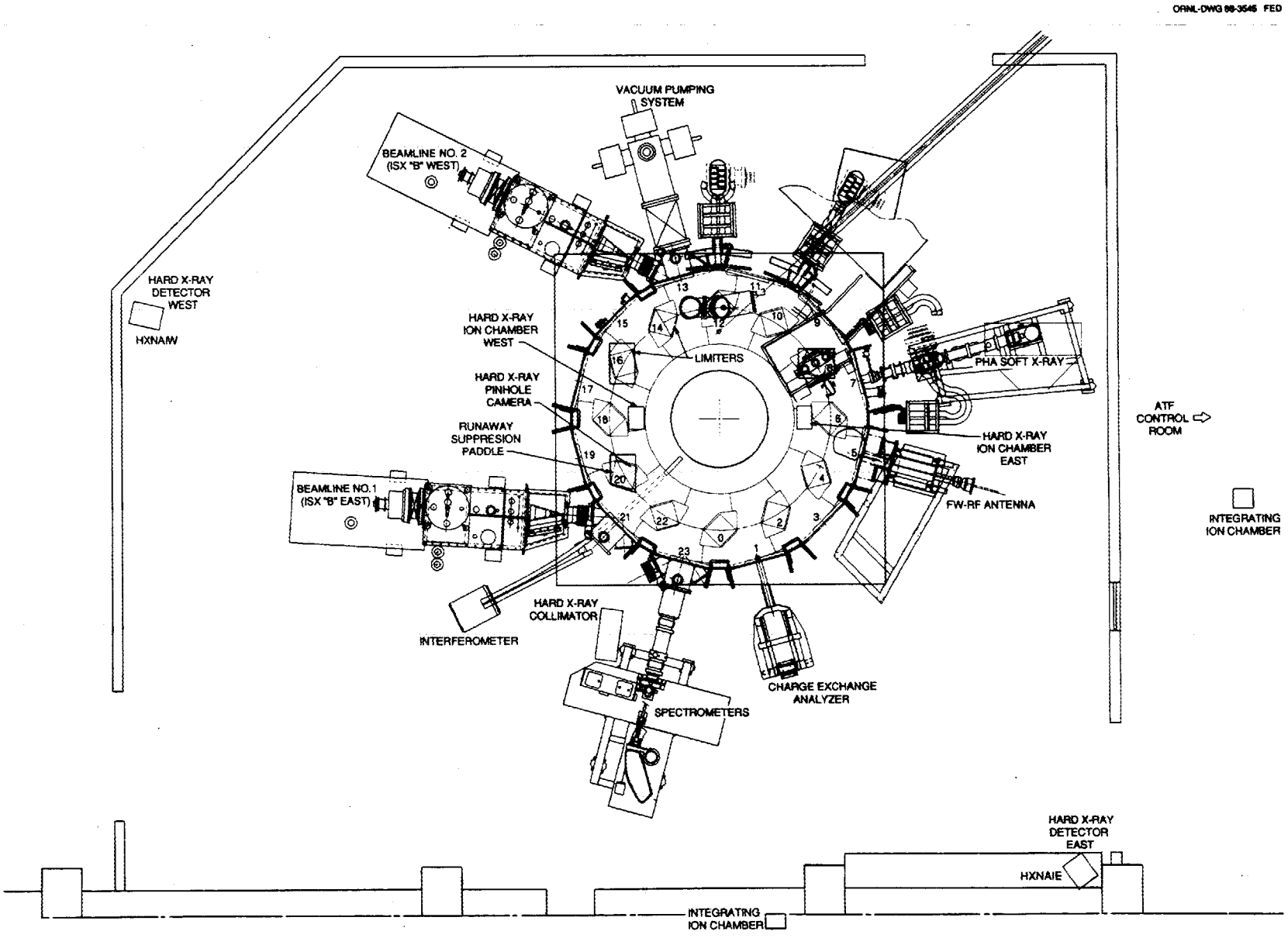


Fig. 6. Plan view of ATF showing the location of the detectors, the runaway suppression paddle, and the control room.

3. Two integrating ionization chambers in occupied areas that were programmed to give the dose per shot.
4. Many pocket ionization chambers, which could be placed at numerous locations in the ATF enclosure as well as in the occupied areas. These could be read after each shot, at the end of a series of shots, or at the end of the day's operation.
5. Many thermoluminescent dosimeters (TLDs), which could also be placed in the ATF enclosure or in occupied areas. These required a day's delay before reading to allow aging of the crystalline material.
6. An NaI(Tl) scintillator in a Pb collimator used in the pulse mode to measure the bremsstrahlung spectra from the parts of ATF that were struck by the runaway electrons.
7. A Pb pinhole camera used to locate the sources of X rays inside ATF. The camera viewed the inside of the vacuum vessel through either a glass window or a thin (0.0508-cm) aluminum window.

Items 1, 2, 6, and 7 are shown in Fig. 6. The locations of the various other items (TLDs, pocket dosimeters, etc.) changed from time to time.

Current flowing from the paddle to the vacuum vessel was measured by monitoring the voltage across a resistor connected between them. The paddle could also be biased relative to the vacuum vessel. However, current measurements and bias experiments were not made in the initial stages of the experiment.

Plasma density was monitored by a standard 2-mm interferometer, which viewed the plasma across the midplane over a 65-cm plasma path length. In addition to the standard fringe counter display of the density waveform, the sine and cosine of the signal could be combined to give an arc tangent signal to display very low plasma densities.

A set of magnetic loops encircled the plasma and included a Rogowski loop from which plasma current signals could be obtained. The sensitivity was such that plasma currents of much less than $\sim$1 kA could not be observed. In the earliest phase of the experiment, a simple electron cyclotron emission (ECE) diagnostic was installed with a fixed frequency. The system consisted of an existing large waveguide (used for electron cyclotron resonance discharge cleaning), a taper to a WR-15 waveguide, a crystal detector, and a single-ended mixer with a logarithmic amplifier. The system was set for 26.5 GHz with a 70-MHz bandwidth. The plasma density for cutoff was $8.7 \times 10^{18}$ m$^{-3}$.

# 5. MEASUREMENTS

## 5.1 HARD X-RAY INTENSITY

For nonoptimum vertical field programming (i.e., with the trim field ramped up simultaneously with the helical field), Fig. 7(a) shows typical time behavior of the hard X-ray signals (inverted) as related to the loop voltage generated by the ramping of the two fields.

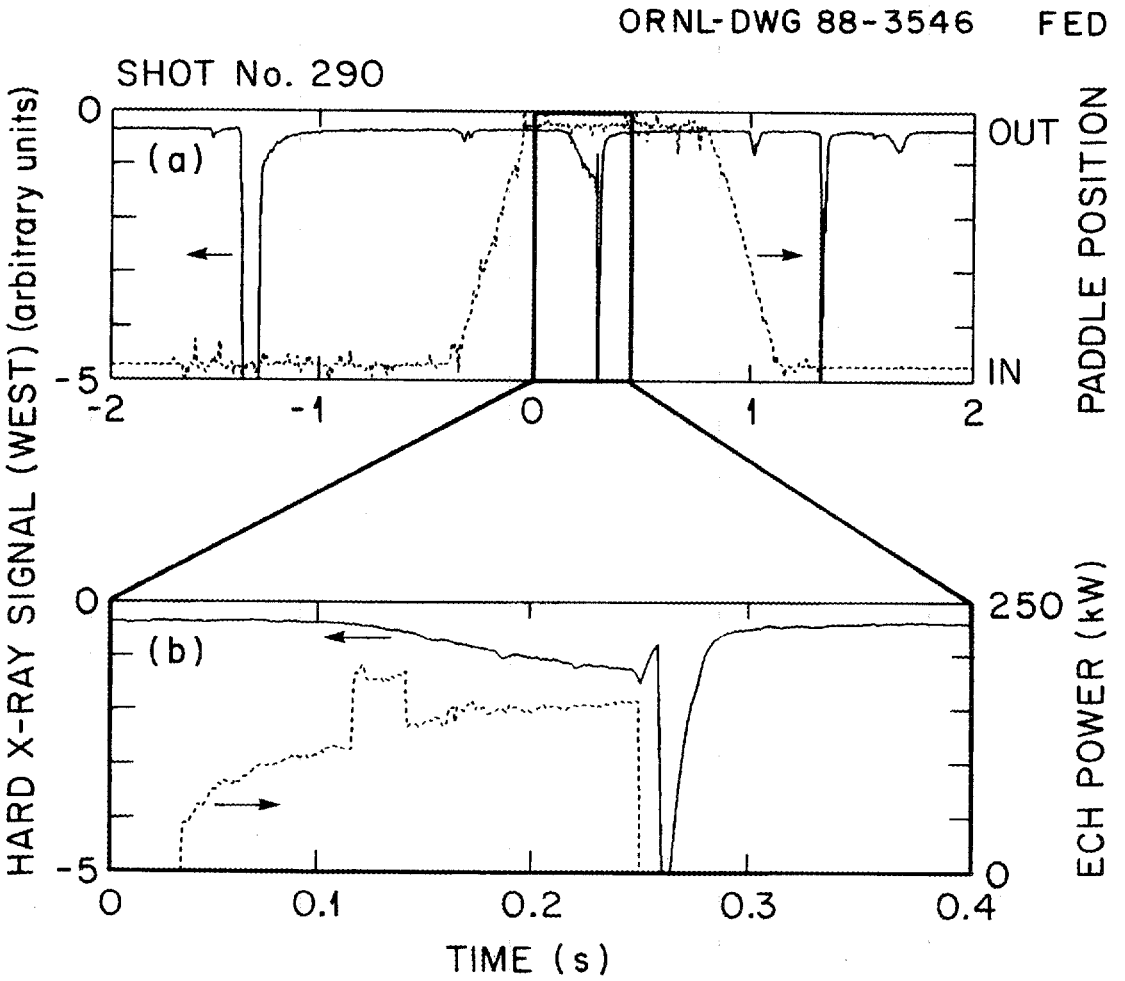


Fig. 7. Typical time behavior of the hard X-ray signals with nonoptimum vertical field programming (i.e., the trim field ramped simultaneously with the helical field): (a) the entire duration of the shot and (b) the ECH portion showing the hard X-ray signal during and immediately following the ECH.

There are bursts at the time of the helical and vertical field ramp-up and ramp-down. It should be emphasized that these are typical and that not every shot is the same. Often there is no significant X-ray burst on ramp-up. If the helical field does not "flat top" (i.e., reach a constant value), then the residual loop voltage can enhance the X-ray bursts. When the plasma contains a high concentration of impurities or when a residual loop voltage is present, the hard X-ray signal often increases during the ECH pulse and one or more X-ray bursts follow the ECH signal. Figure 7(b) shows an expanded trace of the X-ray signal (inverted) during and after the ECH pulse under such conditions. Generally, after a long period of plasma operation and discharge cleaning, no X-ray burst occurs during and immediately after the ECH pulse.

Measurements show a small loop voltage during the flat-top portion of the helical field. This voltage is sufficient to drive a small toroidal current and may be responsible for maintaining runaway electrons, which are accelerated by the ECH. The instabilities observed are similar to those observed on Uragan-2[14–16] during ohmic heating with very small toroidal electric fields. However, it is possible that the X rays observed during and after the ECH pulse are due not to toroidal runaways but to trapped electrons accelerated by the ECH.

The runaway suppression paddle sometimes produces a burst of X rays as it begins to move outward and again as it returns to the center of the chamber. This is particularly true if the paddle position is not optimized and/or if a residual loop voltage exists. Such bursts are observed at approximately $-0.5$ s and 1.0 s in Fig. 7(a). Small adjustments in the radial position of the paddle can reduce this burst depending on the value of the vertical trim field and the inner vertical field.

A strong reduction of X-ray intensity has been produced by careful timing of the vertical fields, as was discussed in Sect. 3. Figure 8(a) shows the X-ray intensity (inverted) for a shot before (shot 753; solid line) and a shot after (shot 754; dotted line) delaying the timing of the vertical fields by 200 ms so as to keep the drift surfaces as far out as possible during the main helical field ramp-up. Figure 8(d) shows the trim vertical fields for the same two shots. Not only are the bursts at the times of current ramping absent, but also the burst at the time of the ECH pulse is missing.

During the flat-top phase prior to plasma production by ECH, under non-optimum conditions with a relatively high residual loop voltage and dirty plasma

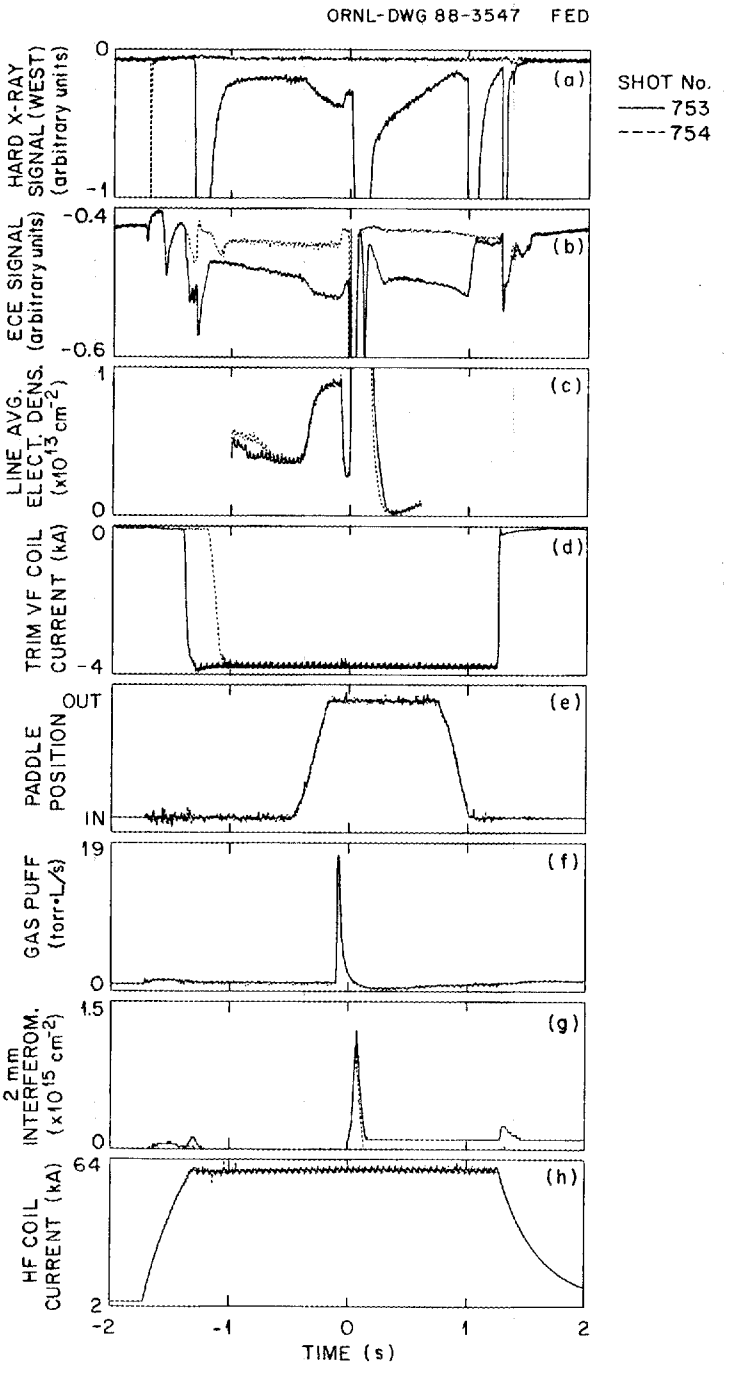


Fig. 8. Time behavior of (a) hard X rays, (b) ECE signal, (c and g) electron density, (d) trim vertical field, (e) paddle position, (f) gas puff, and (h) helical fields for nonoptimum field programming (shot 753, solid line) and optimum field programming (shot 754, dotted line).

conditions, the runaways are observed to produce X-rays when they strike the paddle. Figure 9(a) shows the hard X-ray intensity (inverted) as a function of time correlated with the paddle motion [Fig. 9(b)]. The large X-ray bursts occur at helical field ramp-up and ramp-down. The small bursts of X rays appearing after $\sim -1.2$ s disappear during the transit of the paddle from the center to the wall of the

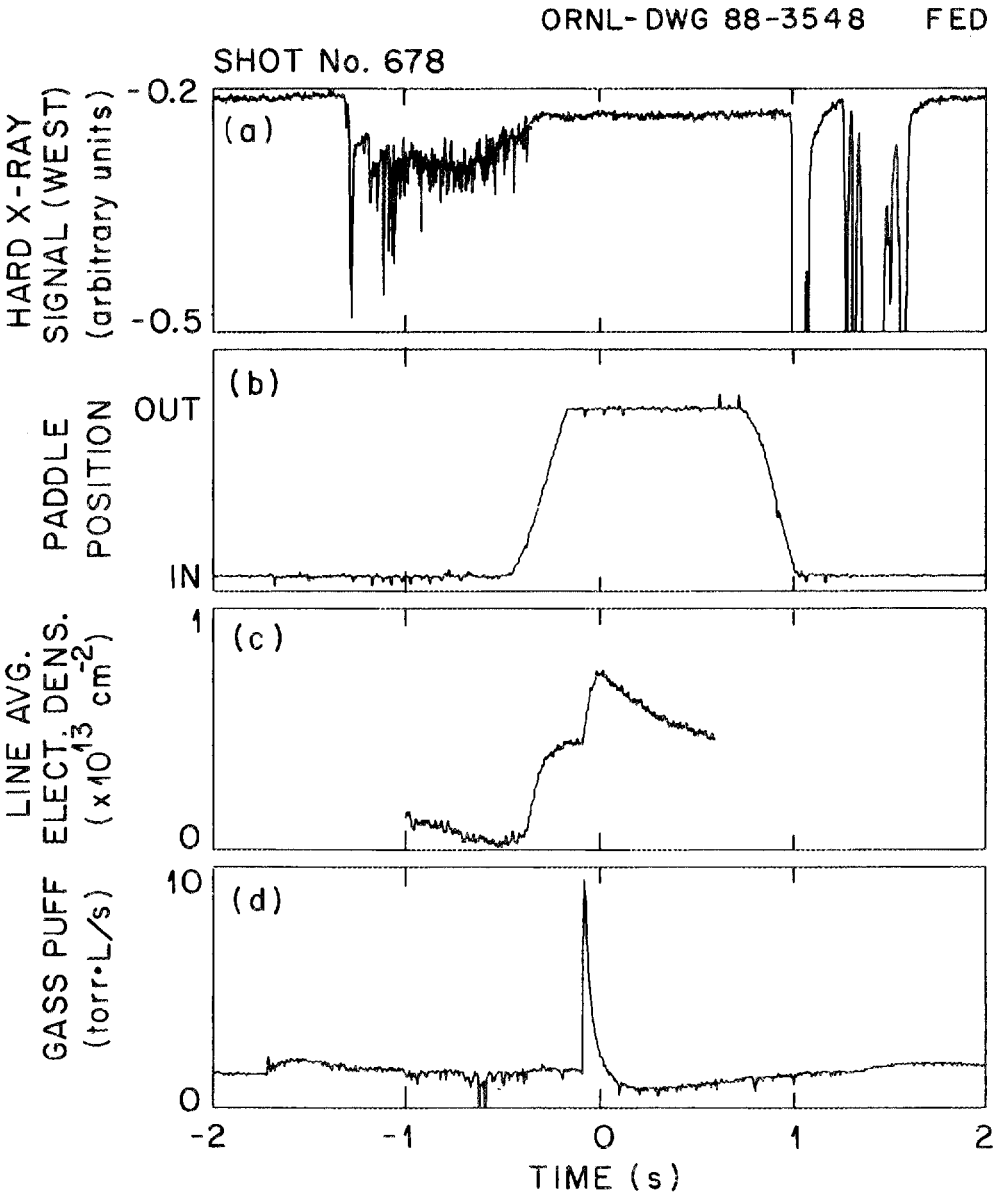


Fig. 9. Hard X-ray temporal behavior correlated with paddle motion during conditions of high residual loop voltage and impure plasma conditions: (a) hard X-ray signal, (b) paddle position, (c) $n_e\ell$, line density, and (d) gas puff.

vacuum chamber. One inference from this is that the paddle and the associated arm do not present a large enough cross section to stop runaway formation completely. Some particles miss the paddle and arm on many successive toroidal transits and strike the paddle only after they have gained enough energy to be detected by the hard X-ray monitor. Figure 9(c) shows the line density increasing as the paddle moves out and increasing again at the time of a small gas puff [Fig. 9(d)]. There was no ECH plasma production on this shot.

During neutral beam operation or heavy gas puffing, the ramp-down X-ray intensity is strongly reduced. This may be caused by the reduction of runaways by the Langmuir turbulence generated by the high loop voltage as was observed in Uragan-2.[16]

## 5.2 ECE AND 2-mm INTERFEROMETER DIAGNOSTIC SIGNALS

As mentioned earlier, the ECE diagnostic and the 2-mm interferometer detect evidence of a long-lived component in the plasma. This is illustrated in Fig. 8(b), which shows the ECE signal for two successive shots. The first shot had the trim vertical field programmed to occur near the end of the HF ramp-up. The second had the trim vertical field programmed to occur at the end of the HF ramp-up to hold the drift surfaces radially outward to the maximum extent as long as possible. The ECE signal for the first shot shows a signal that begins to increase at the same time that the runaway paddle begins its outward motion. The small dip in the signal at $-0.1$ s is caused by the gas puff before the ECH pulse. After the ECH pulse, the signal recovers to near the value before the ECH pulse and gradually increases. As the paddle returns to the plasma center at $\sim 1$ s, the signal drops.

The dotted trace shows the signal with the delayed trim vertical field programming. The signal is still detectable, but it is reduced from the previous shot. There is no change with paddle motion; however, a reduction occurs with the gas puff at $-0.1$ s. The signal is much reduced after the ECH pulse, although it does increase gradually with time. Again, no change is seen when the paddle returns to the center.

This appears to be evidence of a superthermal component in the vessel during the entire HF time. It is reduced but not eliminated by the vertical field programming. Because of the presence of a small loop voltage during the helical field "flat top," the superthermal component can be maintained during this time. Despite careful programming of the helical field power supply SCR phasing, it is not possible to remove this loop voltage completely.

Figure 8(c) shows the 2-mm interferometer arc tangent signal for the same shots. The two signals for the shots are virtually identical. However, since the ECE signals were not identical, it would appear that the runaway energy that created the density was considerably higher in the first shot than in the second. The density increases by a small amount as the paddle moves outward at about −0.5 s, decreases at the time of the normal gas puff [Fig. 8(f)], increases strongly when the ECH power comes on at 0 s, and then decreases when the ECH power goes off. Based on the assumption of a 65-cm path length (the distance between the inner and outer $\iota = 1.0$ surfaces), the increase in line-averaged density as the paddle moves out is $\sim 7.7 \times 10^{10}$ cm$^{-3}$. A current of relativistic electrons of ~60–90 mA would have produced an electron density of this magnitude, not including secondary ionization in the background gas. For reference, Fig. 8(d) shows the trim VF current for these two shots, Fig. 8(e) shows the paddle position ("in" is at the bottom and "out" is at the top), Fig. 8(f) shows the gas puff, Fig. 8(g) shows the 2-mm interferometer fringe counter display (which is too insensitive to see the low-density plasma during the flat top), and Fig. 8(h) shows the HF current.

It should be noted that this residual density and the ECE signal are not always present. A fraction (~20–30%) of the shots shows no signals of this type. We have found no obvious correlation with any other process or signal, with the possible exception of one: when the plasma is pushed inward to a smaller major radius than normal by the trim vertical field, this current is almost always present. When the plasma is shifted in, the paddle no longer intercepts any flux or runaways in a small region near the axis with a radius of ~5 cm. This may partially account for the long-lived component. After the ECH-produced plasma has decayed, the ECE signal sometimes returns to a nonzero level, as in Fig. 8(b), and sometimes it does not. If there has been neutral beam injection, it generally returns to zero, indicating probably that the increased gas pressure has prevented formation of an energetic component.

### 5.3 HARD X-RAY ENERGIES

The bremsstrahlung spectra from ATF have been measured by a collimator and detector located on the floor near ATF and aimed at the region of the paddle in sector 20. The collimation is designed to exclude other parts of ATF but to include any object in that region that might be a source of X rays. The detector views

the paddle through the vacuum vessel and structural shell. The $\gtrsim$5 cm of steel in the line of sight helps to reduce the low-energy photon flux and to diminish the possibility of pulse pile-up. The threshold setting on the pulse height analyzer is set between 0.5 and 1.0 MeV to eliminate low-energy photons, which also reduces pulse pile-up. The counting rate is kept below $10^4$ $s^{-1}$. The energy scale is determined by standard radioactive sources ($^{137}$Cs, $^{60}$Co, etc.).

The present operation involves accepting all photons that occur during the ramp-up, plasma operation, and ramp-down (i.e., no attempt has been made to separately examine the ramp-up and ramp-down bremsstrahlung during a single discharge). However, individual shots with only ramp-up or ramp-down bremsstrahlung have been selected. The collimator line of sight makes an angle of 40° with the horizontal. For the normal counterclockwise (CCW) helical field direction, the collimator observes only photons that are emitted at ~140° from the initial electron velocity direction. When ATF is operated with clockwise (CW) helical fields, the electrons are accelerated in the opposite direction during ramp-down. In this case, the collimator observes photons emitted at ~40° to the initial electron velocity direction. Figure 10 shows typical spectra obtained for ramp-down hard X rays for CCW [Fig. 10(a)] and CW [Fig. 10(b)] operation. The maximum X-ray energy observed for the CCW operation is ~6 MeV. The maximum X-ray energy observed for CW operation is ~12–15 MeV. The maximum photon energy from thick-target bremsstrahlung is a function of the angle of emission, and the flux at a given energy at backward emission angles is strongly reduced.

To date, the detector has not been used to measure spectra during a helical field abortion when the paddle is not in place. Under such conditions, the energy might reach several tens of mega-electron-volts, the intensity would be much larger, the paddle would not be the source, and the detector would probably be saturated. Also, the detector has not been used to measure spectra from the ECH portion of the discharge. Since the location of the emission is also no longer the paddle and the exact source is unknown, there is currently no way to make such a measurement.

A simple measurement of the upper limit of the runaway energy has been made by checking the paddle and other parts of the vacuum vessel for activity. No detectable beta or gamma activity has been observed on any part of the vacuum vessel known to have been a source of bremsstrahlung X rays. Activity can result from photonuclear processes [e.g., ($\gamma$, n), ($\gamma$, p), etc.] for electrons that produce X rays when striking the material surfaces with an energy higher than the threshold for

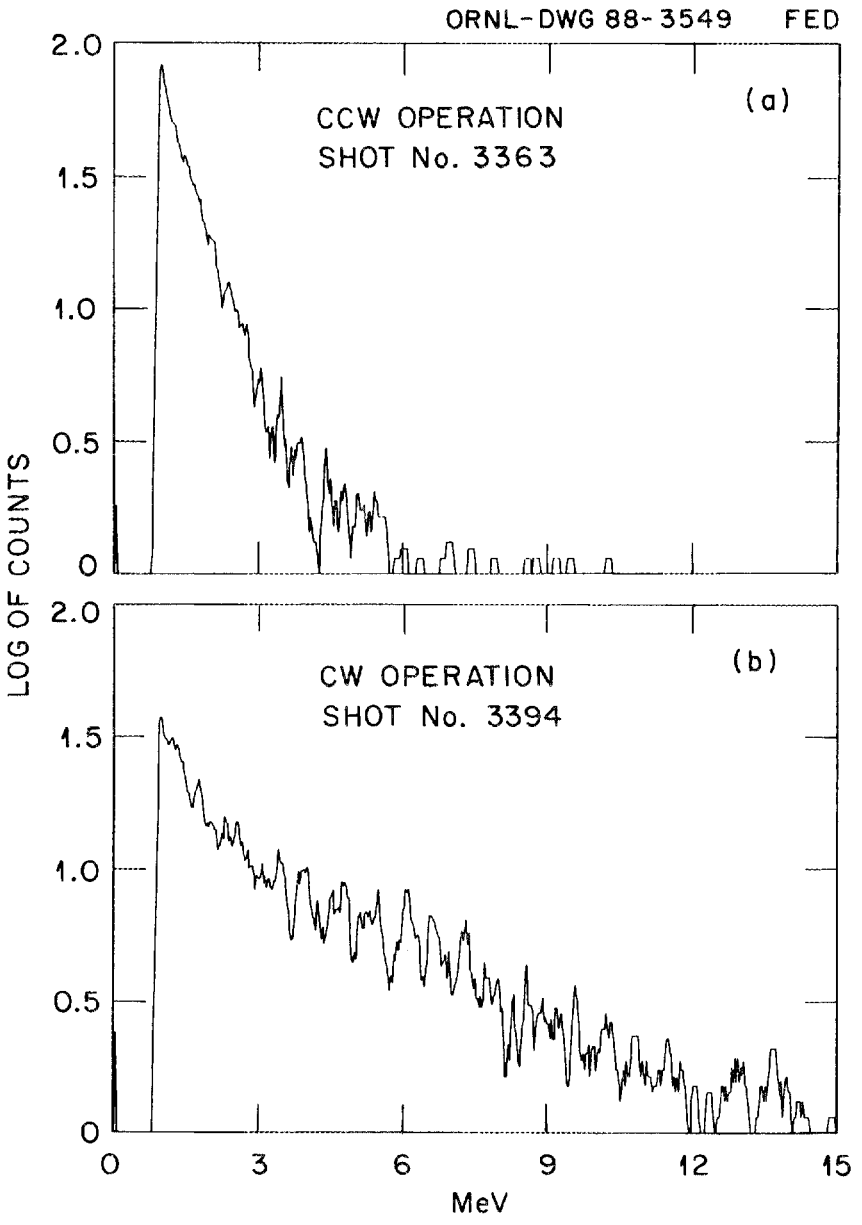


Fig. 10. Bremsstrahlung spectra from ATF for (a) CCW operation and (b) CW operation. In (a) the angle between the initial electron direction and the collimator is ~140°; in (b) the angle is ~40°.

the required reaction. Appendix A contains a table of most of the photonuclear reactions that can occur in 304L stainless steel and that could have produced observable activity in the paddle or wall. Not included in the table are reactions that require a threshold energy $> 25$ MeV. Appendix A also contains a calculation of the lower limit of the current of 10- to 14-MeV electrons, which would have to have been present over the $\sim$700 shots prior to the activity measurement to have produced observable activity. The conclusion is that no significant current of electrons exceeding 12 MeV was present.

Another technique has been used to give a qualitative assessment of the mean X-ray energies. Pocket dosimeters were placed in Lucite "buildup caps" near the west side of ATF where the X-ray intensity was highest. Buildup caps are cylinders or cubes made of a material simulating tissue that permit electronic equilibrium of secondary electrons to be established from a source of high-energy $\gamma$ rays. A series of measurements showed that a buildup cap with 2-cm-thick walls caused the dosimeter readings to be 24% to 29% higher than readings on adjacent bare dosimeters, while a 5-cm-thick buildup cap caused the dosimeter readings to be 7% to 13% higher than readings on adjacent bare dosimeters. Comparing these results to standard buildup tables[17] gives mean X-ray energies of between 0.5 and 1 MeV for the 2-cm cap and between 3 and 6 MeV for the 5-cm cap. The thicker cap would be expected to indicate a higher mean X-ray energy because of the greater range and higher probability of interaction of the higher-energy photons in the thicker material.

## 5.4 PADDLE CURRENT

During the first phase of the experiment, current to the paddle was not monitored. Later, however, the current between the paddle and the vacuum vessel was measured by monitoring the voltage across a small resistor between the insulated paddle and the vessel. Large currents are usually observed during ramp-up and ramp-down of the helical and vertical fields, and if hard X rays are generated, there is excellent correlation between the existence of hard X-rays and the existence of paddle current. The maximum currents are $<1$ A unless the paddle is biased. During the flat-top between the first field ramp and the time the paddle begins to leave the center of the chamber, hard X rays [Fig. 11(a)] and an associated paddle current [Fig. 11(c)] occasionally appear. Both disappear when the paddle [Fig. 11(b)] leaves

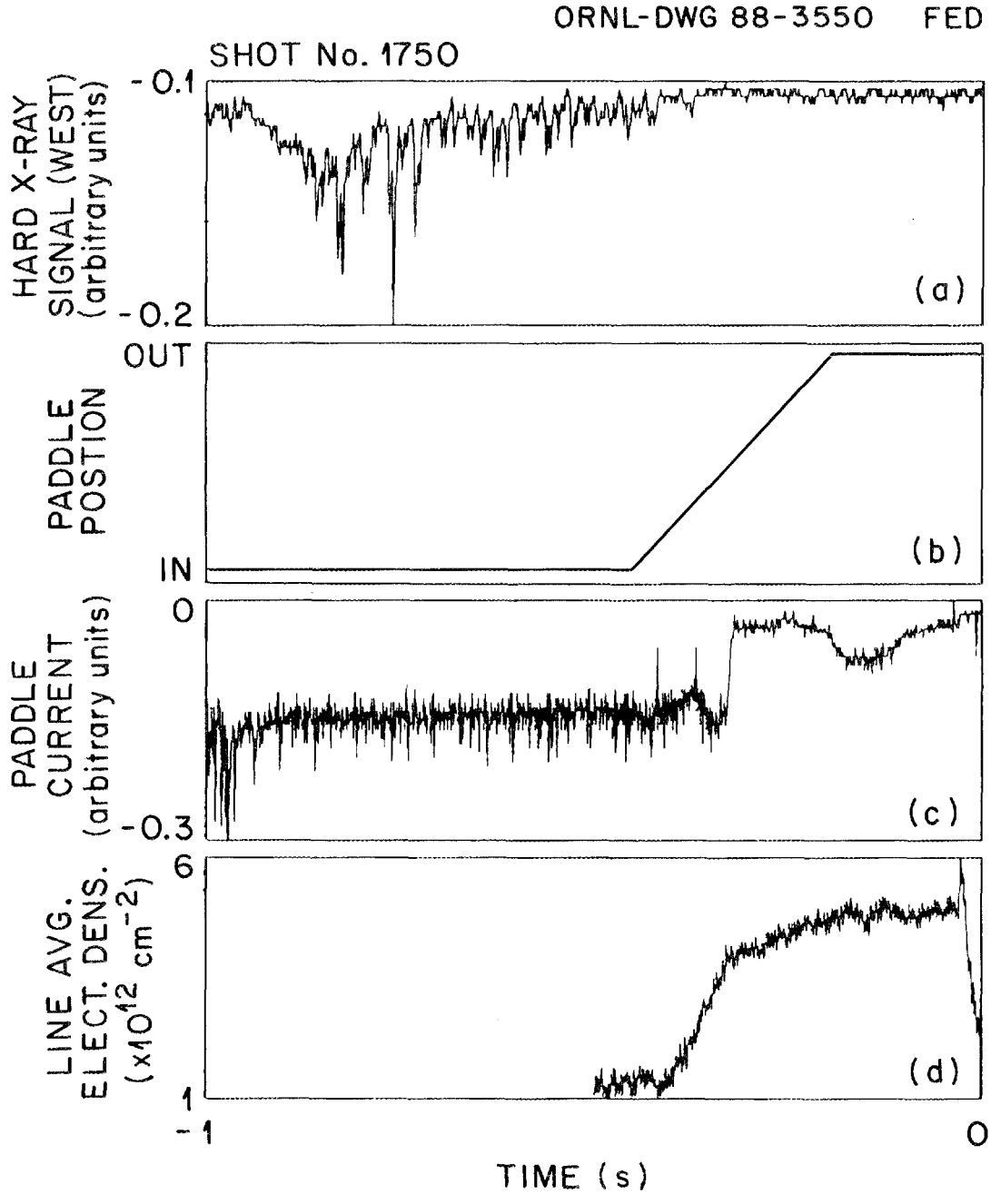


Fig. 11. Time sequence of hard X-ray emission and paddle current for a typical shot with a residual plasma density: (a) hard X-ray signal, (b) paddle position, (c) paddle current, and (d) line-averaged electron density.

the chamber. As the paddle moves out, the interferometer signal often increases, as observed in Fig. 11(d).

Generally, no clear correlation exists between the small current spikes on the paddle and the small hard X-ray spikes. A spectrum analysis of both the X-ray and the paddle current signals shows strong peaks at 30 Hz and its harmonics, with a strong peak at 360 Hz, the frequency of the strongest oscillation on the helical and vertical fields. During the flat-top, whenever there is a low-density plasma $\gtrsim 3 \times 10^{10}$ cm$^{-3}$, a current to the unbiased paddle of $\sim$10 mA almost always exists. If the low-level plasma density is not present on the flat-top, then the paddle current is $\sim$0. We take the lack of correlation of hard X-ray and paddle current fluctuations as evidence that much of the paddle current is not from relativistic electrons. However, the fact that both signals disappear as the paddle moves out indicates that the paddle current has an energetic component that is primarily responsible for the X rays.

## 5.5 PLASMA CURRENT SIGNALS

Measurements made with a Rogowski coil have shown toroidal plasma currents during the ramp-up and ramp-down periods with magnitudes of >10 kA and duration of several tenths of seconds. The current reverses direction from ramp-up to ramp-down as expected because of the reversed loop voltage. Figures 12(a) and 12(b) show the current as a function of time for the same two shots displayed in Fig. 8. Within the sensitivity of the measurement ($\gtrsim$1 kA), no current is apparent during the flat-top. The plasma current signals are usually large during the hard X-ray bursts, indicating that some of the current is caused by runaways.

## 5.6 EFFECT OF DIRECTION OF HELICAL FIELD CURRENT

The distribution of the X-ray intensity and dose is a function of the HF direction. This comes about because of the direction of the induced loop voltage on current ramp-up and ramp-down. The energy of the runaway electrons is high enough so that the bremsstrahlung produced is somewhat peaked in the forward direction. Hence, the direction of the electron path reverses the direction of the radiation if the electrons strike the same object during CW and CCW operation. The direction of the electrons is changed during ramp-up and ramp-down. Since most of the

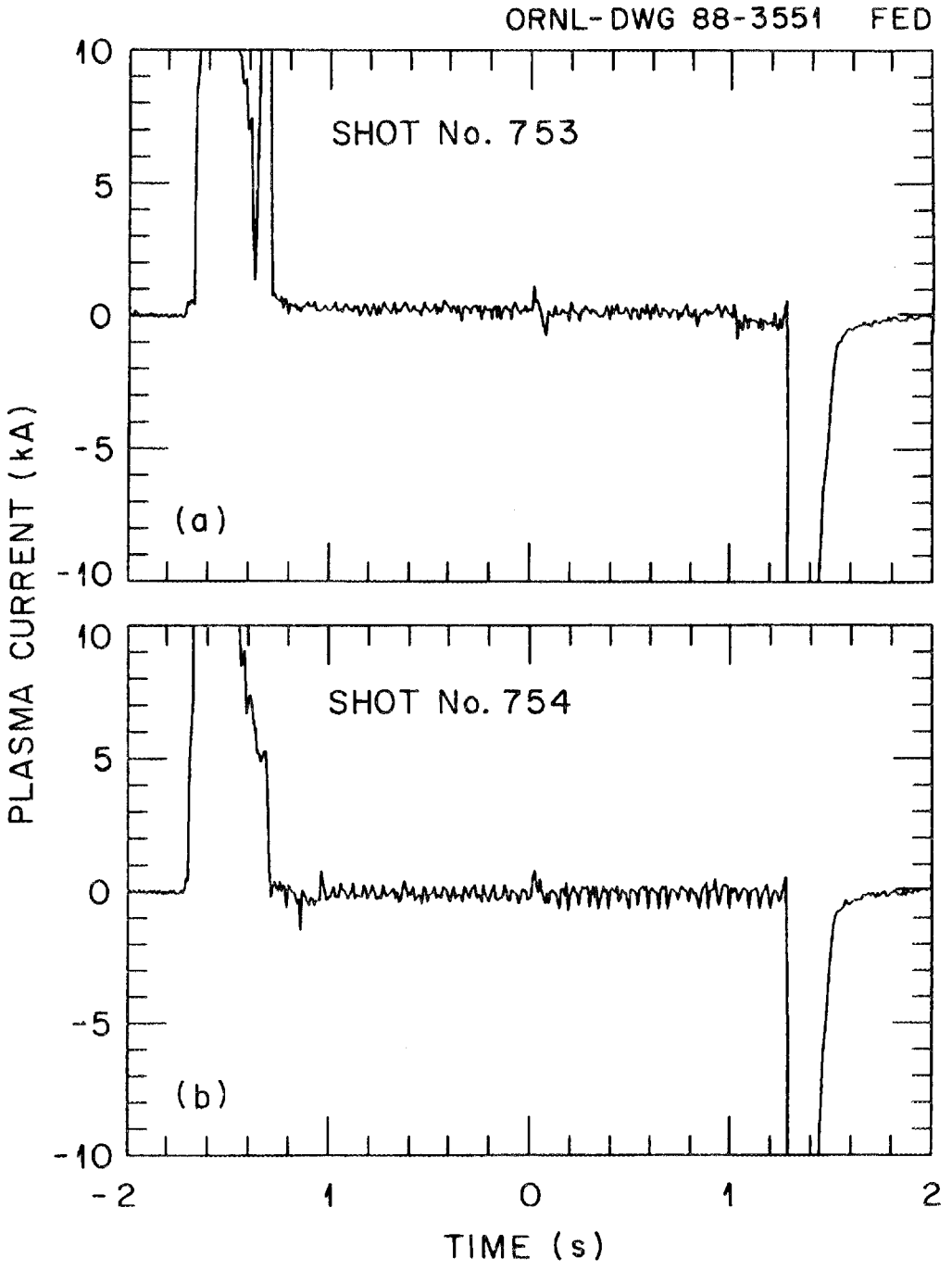


Fig. 12. Plasma current signals for (a) nonoptimal and (b) optimal vertical field programming.

radiation is produced during ramp-down, the intensity distribution is considerably altered between ramp-up and ramp-down.

The pocket dosimeters and TLDs, both of which are integrating devices, primarily measure the ramp-down X-ray dose. Dosimeters placed at the center of each of the outside ports are normally used to give a qualitative assessment of the dose near ATF. A polar intensity plot can be generated from the readings, and, while this does not truly represent the angular distribution of the radiation (due to the internal shielding inside ATF), it can generally indicate the regions where the runaways are striking the vessel and internal components.

Figures 13(a) and 13(b) are polar plots of dosimeter readings for ATF operation with the HF current in the CCW and CW directions, respectively. The plots are normalized to the same maximum intensity since they represent differing numbers of shots during the two kinds of operation. The X-ray dose is highest near ports 19, 20, and 21 and lower near ports 14 and 16. The runaway suppression paddle is in port 20. The biggest peak between CW and CCW operation seems to reflect about a vertical plane through port 20. For CW operation, the dose is higher in port 21 when the ramp-down electron direction is CCW; for CCW operation, the dose is higher in port 19 when the ramp-down electron direction is CW. It appears that the limiters in ports 14 and 16 are not strong sources of radiation (i.e., not many runaway electrons strike the limiters).

There appears to be a smaller peak on the northeast side, which reflects about a vertical plane through port 8 or 9, peaking at port 11 for CCW operation and at port 6 for CW operation. The implication is that an object in the vicinity of port 8 or 9 is serving as a target for the runaways.

TLDs were placed in an array on the wall directly south of port 23. Measurements were taken after a period of operation with CW helical fields so that the bremsstrahlung from the region of sector 20 would be directed toward this wall. The resulting broad distribution of doses over the array can be interpreted as an indication of (1) directivity towards the wall and (2) a mean photon energy that is not very high (which would produce a very narrow cone of intensity). On subsequent days with the helical field reversed, the same array of detectors showed essentially background levels, again indicating that the electron direction for the primary dose is reversed and that the radiation is not aimed toward this wall.

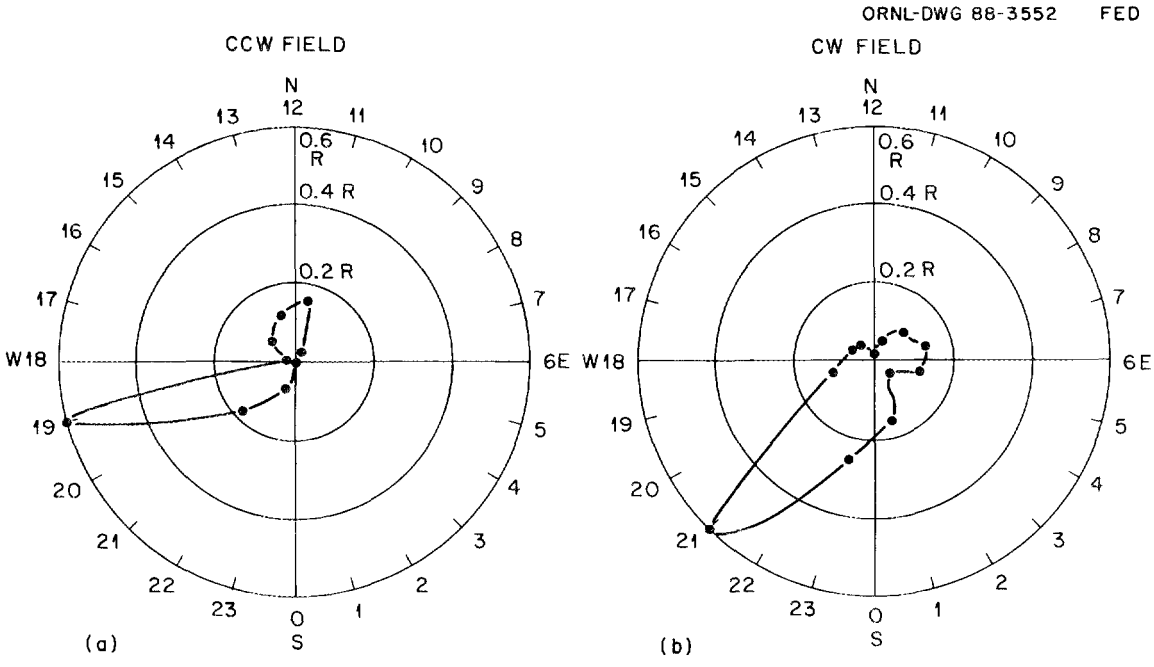


Fig. 13. Polar plot of dosimeter readings from ATF with (a) CCW and (b) CW operation.

## 5.7 LOCATION OF X-RAY SOURCES

X-ray pinhole cameras have been used to locate the source of X rays inside ATF. Again, the measurements are made over the course of many shots, and hence the effects are integrated. A pinhole camera located on the outside of port 19 viewed the interior of ATF through a glass window. When the camera was oriented to view the limiter region, no exposure could be detected. When it was oriented to view the paddle, a strong image was obtained, but scattering in the glass prevented any detail of the paddle from being observed.

A pinhole camera mounted on a thin window on the inside of port 19 could view the large outer flange 19, the magnetic loops, the outer walls of sectors 18 and 20, and the paddle when it was resting against the outer wall (i.e., when the paddle was withdrawn from the plasma). The photos show only a general broad distribution and no specific object on the wall that would be a source of X-rays. We conclude that the magnetic loops are not sources of bremsstrahlung and that, when the paddle is retracted against the wall, it is not struck by the runaways and hence is not a source of bremsstrahlung.

A pinhole camera mounted in a top port of sector 20 viewed the plasma region and the paddle when inserted into the vacuum vessel. From this position, the photographs show one small spot at the location of the paddle and no other images. The spot is always blurred toward the inside of the torus; this is apparently caused by the fact that the paddle bounces when the rotating part strikes the mechanical stop, hence momentarily entering the region $R \lesssim 2.1$ m where it can intercept additional runaways. We conclude from this that the major source of bremsstrahlung in the vacuum vessel in the region of the paddle and magnetic loops is, in fact, the paddle. Because of the insensitivity of the technique, we cannot rule out sources that are present only on occasional shots.

TLDs were inserted between the vacuum vessel and the coils in a number of locations between the top and bottom ports. It is not possible to place the TLDs at every toroidal location because of a variety of interferences. In particular, it is not possible to place them between the top and bottom ports at all 12 locations having such ports; hence, a survey made in this way must necessarily be incomplete. The TLDs again integrate the dose over a number of shots. TLDs inserted near the upper and lower limiters showed no peaking in the vicinity of the limiters, with the limiters set at $\pm 35$ cm from the midplane. However, TLDs inserted near sectors 20 and 18 showed strong peaking on the outside, particularly near the runaway suppression paddle and its arm up to the top port of sector 20.

As an example of these measurements, Fig. 14 shows the distribution of TLD readings on three sectors of ATF with CCW operation so that the runaway electron direction was CW. The TLD readings on port 20 are highest on the outside near the paddle and arm and are also fairly high on the inside of the port. The TLD readings on port 18 in the direction of the bremsstrahlung from the paddle are also high on the outside, as would be expected. Very small doses were detected by the TLDs on sector 14, which contains the upper limiter, but this is also in the general direction of the X rays from sector 20 from the ramp-down.

We can conclude from these TLD measurements that there appears to be a major source of X rays in the vicinity of the paddle. Clearly, other sources may exist, and their location does appear to vary depending on plasma conditions and magnetic configurations.

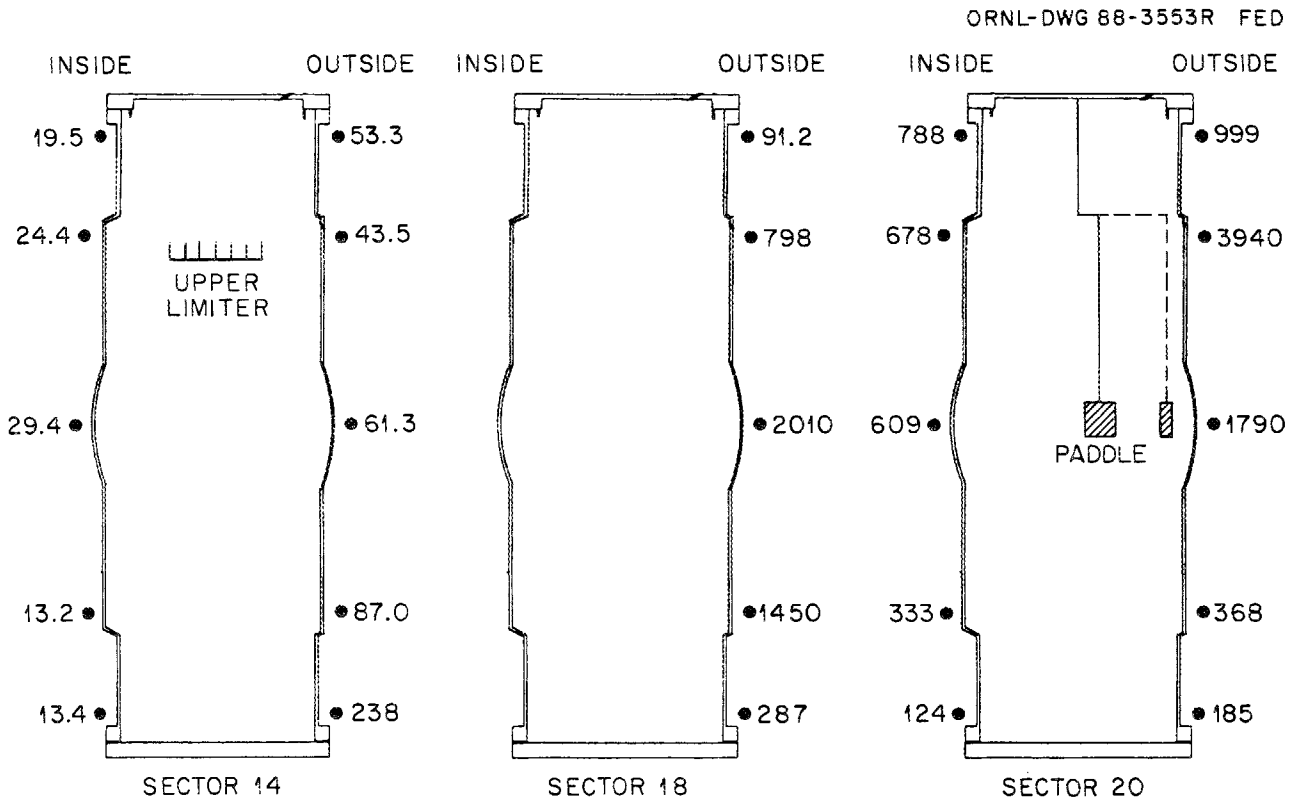


Fig. 14. Dose readings for TLDs inserted between the vacuum vessel and the HF coils for CCW operation.

## 5.8 LIMITER POSITION SCANS

The X-ray intensities were examined during a scan of the top and bottom limiters. For this experiment, the limiters were initially positioned 45 cm from the midplane (i.e., the top was 45 cm above and the bottom was 45 cm below). They were both moved inward by 2-cm steps in a series of successive shots until they were 31 cm from the midplane, which is the limit of travel. At this distance, the limiters were approximately at the $\iota = 0.6$ surface. The last closed flux surface ($\iota = 1.0$) is intercepted by the limiters when they are located at 39 cm.

The hard X-ray intensity on the two west monitors was observed to decrease very slightly initially and then to increase sharply as the limiters reached 31 cm. The current to the paddle also decreased very slowly during this scan. Since the relativistic electrons are expected to be shifted out in the vicinity of the midplane and are not expected to have large vertical excursions, this effect is to be expected. This showed that the relativistic electrons are located vertically within 31 cm of the midplane.

# 6. EFFECTIVENESS OF FIELD PROGRAMMING AND PADDLE USE

The effectiveness of the runaway suppression paddle was measured by comparing two successive shots where an effort was made to generate the worst possible X-ray dose without the paddle and then to leave all other conditions the same but use the paddle to reduce the runaway population. The worst possible situation occurs when a helical field ramp-down occurs directly after the ECH pulse has produced a plasma in the vacuum chamber. The paddle cannot be effective in this case because it is moving too slowly to enter the chamber to intercept the runaways in the event of an abort directly after the ECH plasma.

In the first shot, the paddle was intentionally disabled and left against the vacuum chamber wall. The second shot had the paddle intentionally disabled but located in the center of the vacuum vessel. For this study, only one of the on-line detectors was not saturated; however, dose monitors in the occupied areas were also operating and not saturated. The ratio of the total doses for these two shots delivered to the ionization chamber on the east side of ATF was ~3000:1 for this study. The two integrating detectors in the occupied areas showed measurable doses for the first case but background for the second. They showed, respectively, a

reduction of $\gtrsim$100 in one area and $\gtrsim$40 in the other. This comparison showed that the paddle was very effective in reducing runaway current and personnel dose.

## 7. SUMMARY AND CONCLUSIONS

Pulsed torsatrons and heliotrons are susceptible to runaway electron formation and the resulting hard X-ray radiation because of the inherent good containment in the vacuum fields and the high loop voltages during helical and vertical field ramping. Measurements of hard X rays from ATF have shown that the runaways are produced primarily during field ramping but that usually a small steady-state runaway component is also present during the "flat-top" portion of the fields. A runaway suppression system consisting of a rotating paddle has proved to be very effective in reducing the runaway population. The paddle is the major source of bremsstrahlung, although other objects in the vacuum chamber also serve as targets at various times. The maximum X-ray energy has been determined from pulse height analysis to be about 12–15 MeV. The mean energy appears to be a few mega-electron-volts. There is a noticeable forward peaking of the bremsstrahlung from the paddle. When in the normal operating position, at a radius of 39 cm or more, the limiters do not appear to be major sources of bremsstrahlung.

## ACKNOWLEDGMENTS

We gratefully acknowledge advice from and useful discussions with O. Motojima, H. Kaneko, H. Okada, K. Uo, T. Mizuuchi, and S. Besshou, Kyoto University, Uji, Japan, concerning many aspects of the operation of Heliotron-E. The authors have benefited greatly from discussions with S. M. Hamberger, Australian National University, Canberra, Australia, concerning torsatron operation and N. Perepelkin, Kharkov Physical-Technical Institute, U.S.S.R., concerning runaway electrons during ohmic heating in stellarators. We acknowledge valuable service and support from members of the ATF operations staff: J. L. Yarber, G. R. Dyer, J. W. Halliwell, and G. H. Henkel. We acknowledge the services of D. S. Colwell, T. A. Rhea, and R. E. Halliburton of the ORNL Environmental and Occupational Safety Division for calibration of the pocket dosimeters and reading and interpretation of the TLDs.

## REFERENCES


1. J. F. Lyon et al., *Fusion Technol.* **10**, 179–226 (1986).
2. G. H. Neilson et al., *Europhys. Conf. Abstr.* **12D**(II), 486 (1988).
3. M. J. Saltmarsh et al., in *Proceedings of the 12th International Conference on Plasma Physics and Controlled Nuclear Fusion Research, Nice, France, October 12–19, 1988*, IAEA, Vienna (to be published).
4. S. Besshou, O. Motojima, A. Iiyoshi, and K. Uo, *J. Nucl. Sci. Technol. (Japan)* **19**, 821–30 (1982).
5. O. Motojima and members of Heliotron-E staff, private communications, 1987 and 1988.
6. W. Bernstein, F. F. Chen, M. A. Heald, and A. Z. Kranz, *Phys. Fluids* **1**, 430 (1958).
7. R. Motley, C. P. Lustig, and S. Sanders, *J. Nucl. Energy* **3**, 17 (1961).
8. E. B. Mersevey and L. P. Goldberg, *Phys. Fluids* **4**, 1307–14 (1961).
9. P. I. Blinov and L. P. Zakatov, *Plasma Phys.* **8**, 447–53 (1966).
10. O. S. Pavlichenko, F. F. Tereshchenko, and V. M. Tonkopryad, *Sov. J. Plasma Phys.* **3**, 180–4 (1977).
11. J. H. Harris, *Nucl. Fusion* **24**, 159 (1984).
12. S. Hamberger, L. E. Sharp, A. Malein, J. Bradley, and W. McKay, in *Proceedings of the 5th International Conference on Plasma Physics and Controlled Nuclear Fusion Research, Tokyo, November 11–15, 1974*, IAEA, Vienna, Vol. II, pp. 21–32 (1975).
13. D. A. Rasmussen et al., 'Suppression of X-Rays Generated by Runaway Electrons in ATF," to be published.
14. N. F. Perepelkin et al., in *Proceedings of the 11th European Conference on Controlled Fusion and Plasma Physics, Aachen, Federal Republic of Germany, September 1983*, **D17**, Part I, pp. 243–6, European Physical Society, Geneva, 1983.
15. N. F. Perepelkin et al., *Sov. Tech. Phys. Lett.* **9**, 397–8 (1983).
16. E. D. Volkov et al., *Sov. J. Plasma Phys.* **10**, 409–13 (1984).

17. J. E. Turner, *Atoms, Radiation, and Radiation Protection*, Pergamon Press, p. 256 (1986); A. B. Chilton, J. K. Shultis, and R. E. Faw, *Principles of Radiation Shielding*, Prentice-Hall, Inc., Englewood Cliffs, N.J., Appendix 4, pp. 444–58 (1984).

# Appendix A

## PHOTONUCLEAR REACTIONS PRODUCED BY RUNAWAY ELECTRONS IN 304L STAINLESS STEEL

The vacuum chamber and paddle of ATF are made of 304L stainless steel. All possible photonuclear reactions leading to radioactive daughters that can occur in 304L stainless steel are indicated in Table A-1 for reactions with thresholds below 25 MeV. Reactions with thresholds above 25 MeV have not been included. Such

Table A-1. Possible photoactivation of 304L stainless steel (composition: 0.03% C, $\lesssim$2% Mn, $\lesssim$1% Si, 18–20% Cr, 8–12% Ni, 65–71% Fe)

| Target isotope | Percentage of steel composition | | Reaction | Threshold (MeV) | Half life[a] | Comments |
|---|---|---|---|---|---|---|
| | Elemental | Total | | | | |
| $^{50}$Cr | 4.31 | 0.77–0.86 | $(\gamma, n)^{49}$Cr | 12.93 | 42.1 m | $\beta^+$ |
| $^{50}$Cr | 4.31 | 0.77–0.86 | $(\gamma, p)^{49}$V | 9.59 | 330 d | EC |
| $^{50}$Cr | 4.31 | 0.77–0.86 | $(\gamma, np)^{48}$V | 21.14 | 16.0 d | $\beta^+$, EC |
| $^{50}$Cr | 4.31 | 0.77–0.86 | $(\gamma, 2n)^{48}$Cr | 23.32 | 21.6 h | EC |
| $^{52}$Cr | 83.76 | 15.08–16.75 | $(\gamma, n)^{51}$Cr | 12.04 | 27.7 d | EC, $\beta^-$[b,c] |
| $^{52}$Cr | 83.76 | 15.08–16.75 | $(\gamma, np)^{50}$V | 21.55 | $1.3 \times 10^{15}$ y | EC |
| $^{53}$Cr | 9.55 | 1.72–1.91 | $(\gamma, p)^{52}$V | 11.13 | 3.75 m | $\beta^-$ |
| $^{53}$Cr | 9.55 | 1.72–1.91 | $(\gamma, 2n)^{51}$Cr | 19.98 | 27.7 d | EC, $\beta^-$[b,c] |
| $^{54}$Cr | 2.38 | 0.43–0.48 | $(\gamma, p)^{53}$V | 12.04 | 1.61 m | $\beta^-$ |
| $^{54}$Cr | 2.38 | 0.43–0.48 | $(\gamma, np)^{52}$V | 20.85 | 3.75 m | $\beta^-$ |
| $^{55}$Mn | 100 | $\leq$2.00 | $(\gamma, n)^{54}$Mn | 10.23 | 312 d | EC[b] |
| $^{55}$Mn | 100 | $\leq$2.00 | $(\gamma, 2n)^{53}$Mn | 19.16 | $3.74 \times 10^6$ y | EC |
| $^{54}$Fe | 5.82 | 3.78–4.13 | $(\gamma, n)^{53}$Fe | 13.6 | 8.51 m | EC, $\beta^+$ |
| $^{54}$Fe | 5.82 | 3.78–4.13 | $(\gamma, p)^{53}$Mn | 8.85 | $3.72 \times 10^6$ y | EC |
| $^{54}$Fe | 5.82 | 3.78–4.13 | $(\gamma, np)^{52}$Mn | 20.90 | 5.59 d | EC, $\beta^+$ |
| $^{54}$Fe | 5.82 | 3.78–4.13 | $(\gamma, 2n)^{52}$Fe | 24.06 | 8.27 h | EC, $\beta^+$ |

Table A-1. (continued)

| Target isotope | Percentage of steel composition: Elemental | Total | Reaction | Threshold (MeV) | Half life[a] | Comments |
|---|---|---|---|---|---|---|
| $^{56}$Fe | 91.66 | 59.6–65.7 | $(\gamma, n)^{55}$Fe | 11.2 | 2.73 y | EC |
| $^{56}$Fe | 91.66 | 59.6–65.7 | $(\gamma, np)^{54}$Mn | 20.4 | 312 d | EC[b] |
| $^{57}$Fe | 2.19 | 1.42–1.55 | $(\gamma, p)^{56}$Mn | 10.6 | 2.57 h | $\beta^-$ |
| $^{57}$Fe | 2.19 | 1.42–1.55 | $(\gamma, 2n)^{55}$Fe | 18.84 | 2.73 y | EC |
| $^{58}$Fe | 0.33 | 0.21–0.23 | $(\gamma, p)^{57}$Mn | 11.96 | 1.45 m | $\beta^-$ |
| $^{58}$Fe | 0.33 | 0.21–0.23 | $(\gamma, np)^{56}$Mn | 20.60 | 2.58 h | $\beta^-$ |
| $^{58}$Ni | 68.274 | 5.46–8.19 | $(\gamma, n)^{57}$Ni | 12.2 | 1.50 d | EC, $\beta^{+}$[b,c] |
| $^{58}$Ni | 68.274 | 5.46–8.19 | $(\gamma, p)^{57}$Co | 8.17 | 272 d | EC[a] |
| $^{58}$Ni | 68.274 | 5.46–8.19 | $(\gamma, np)^{56}$Co | 19.6 | 77.7 d | EC, $\beta^+$ |
| $^{58}$Ni | 68.274 | 5.46–8.19 | $(\gamma, 2n)^{56}$Ni | 22.5 | 6.10 d | EC |
| $^{60}$Ni | 26.095 | 2.09–3.13 | $(\gamma, n)^{59}$Ni | 11.4 | $7.5 \times 10^4$ y | EC |
| $^{60}$Ni | 26.095 | 2.09–3.13 | $(\gamma, np)^{58}$Co | 20.0 | 70.9 d | EC, $\beta^{+}$[b] |
| $^{61}$Ni | 1.134 | 0.09–0.13 | $(\gamma, p)^{60}$Co | 9.86 | 5.27 y | $\beta^{-}$[b] |
| $^{61}$Ni | 1.134 | 0.09–0.13 | $(\gamma, 2n)^{59}$Ni | 19.20 | $7.5 \times 10^4$ y | EC |
| $^{62}$Ni | 3.59 | 0.29–0.43 | $(\gamma, p)^{61}$Co | 11.11 | 1.65 h | $\beta^-$ |
| $^{62}$Ni | 3.59 | 0.29–0.43 | $(\gamma, np)^{60}$Co | 20.45 | 5.27 y | $\beta^{-}$[b] |
| $^{64}$Ni | 0.904 | 0.07–0.11 | $(\gamma, n)^{63}$Ni | 9.6 | 100.1 y | $\beta^-$ |
| $^{64}$Ni | 0.904 | 0.07–0.11 | $(\gamma, p)^{63}$Co | 12.48 | 27.4 s | $\beta^-$ |
| $^{64}$Ni | 0.904 | 0.07–0.11 | $(\gamma, np)^{62}$Co | 20.94 | 13.9 m | $\beta^-$ |
| $^{64}$Ni | 0.904 | 0.07–0.11 | $(\gamma, \alpha)^{60}$Fe | 8.1 | $\sim 1 \times 10^5$ y | $\beta^-$ |

[a] s = second, m = minute, d = day, and y = year.

[b] Observed on PLT.[1]

[c] Observed on Heliotron-E.[2]

reactions involve the emission of more than two nucleons [e.g., ($\gamma$, $\alpha$, n), ($\gamma$, d, n), etc.]. All reactions of the form ($\gamma$, $\alpha$) tend to have very low thresholds (~6–9 MeV), but, fortuitously, only one of the daughters for the materials in 304L stainless steel is radioactive. That one, from the reaction $^{64}Ni(\gamma,\alpha)^{60}Fe$, has a threshold of 8.1 MeV but a very long half-life ($3 \times 10^5$ years). Since $^{64}Ni$ constitutes only 0.07–0.11% of the steel, this reaction is probably undetectable.

Some of the data of Table A-1 are plotted in Fig. A-1. Specifically, the product of the mean life (s) and the percentage of the isotope is plotted vs the threshold energy (MeV). This product is a measure of the ability to observe the reaction by measurement of activity in the material. An isotope for which this product is $\lesssim 4 \times 10^5$ s is probably unobservable because of its the short mean life and low percentage composition. An isotope for which this product is $\gtrsim 4 \times 10^9$ s is also probably unobservable because of its very long mean life, which implies that the activity is very low. The graph shows that the activities fall into two groups. A number of isotopes have thresholds between 8.17 and 13.6 MeV. Their activities involve a photonuclear reaction with the emission of one nucleon [e.g., ($\gamma$, n)

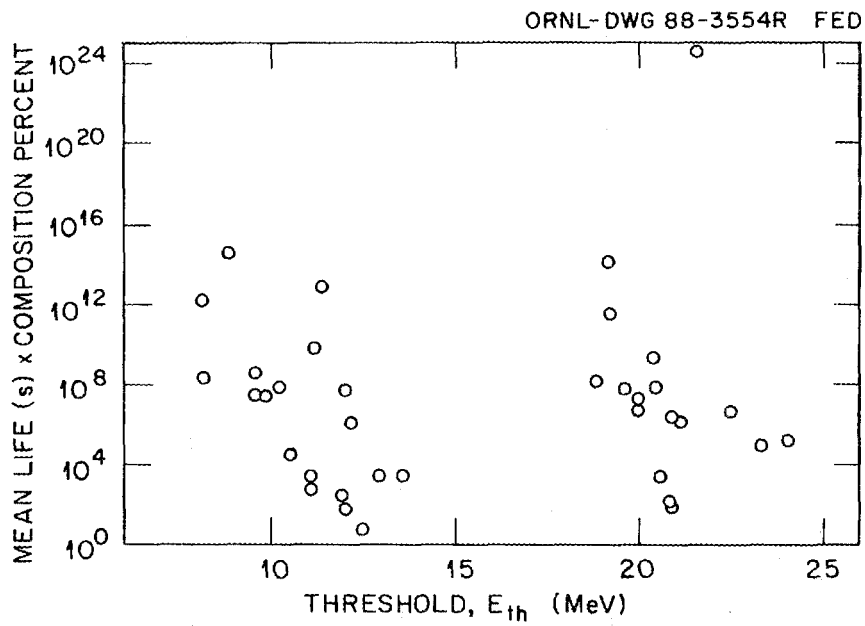


Fig. A-1. Product of the mean life (s) and percent composition of the constituent isotopes of 304L stainless steel vs the threshold for the photonuclear reaction (MeV). The product plotted on the abscissa is a measure of the ability to observe the reaction by measuring the activity of the material.

or ($\gamma$, p)]. A second group of reactions has higher thresholds between 18.84 and 24.06 MeV. These reactions involve the emission of two nucleons [e.g., ($\gamma$, 2n), ($\gamma$, np), etc.]. From Fig. A-1, it is apparent that about eight isotopes in 304L stainless steel have thresholds below 14 MeV and a mean life–percent composition in the above-mentioned range, which gives reasonable probability of producing observable activity if electrons of that energy strike the steel.

An estimate of the total current of electrons with energies above the various thresholds for isotope production can be obtained from the following considerations. The threshold energies are all well known, and some of the photonuclear cross sections are known. In most cases, however, what is known is the integral cross section, $\int \sigma \cdot dE$ (MeV·mb), the integrated cross section from the threshold to the energy of the electron beam producing the activity. With the knowledge that no activity has been observed above background and with an estimate of the solid angle of the detector and its efficiency for the emitted gamma ray activity (or beta activity), an upper limit on the number of active atoms of that isotope can be estimated. This activity would have been acquired in the ~700 shots prior to the examination of the paddle, the magnetic loops, and the interior of the vacuum vessel. This number includes all shots with field ramps as well as those with plasma production and heating by auxiliary means. The total fluence of photons above the threshold can be calculated from the maximum activity, the total number of target atoms available to be made active by the photonuclear process, and the integral cross section.

The following equation relates these quantities:

$$N = F \cdot nV \cdot \int \sigma \, dE/(E_e - E_{th}) \, ,$$

where $N$ is the total number of active atoms produced in the target by energetic photons above the threshold, $F$ is the fluence of photons above threshold (number/cm$^2$), $n$ is the density of target nuclei of the specified isotope, $V$ is the target volume, $E_e$ is the electron energy, and $E_{\rm th}$ is the threshold energy.

The fluence of photons can be related to the integrated power of the electrons incident on the target by the following argument. For a given material, the fraction of energy converted to bremsstrahlung photons is given by Koch and Motz[3] as

$$P_{\rm tot} = 1 \times 10^{-3} Z(E_e - k) \, ,$$

where $Z$ is the atomic number, $E_e$ is the electron energy, and $k$ is a constant. For the target, we take $Z = 26$ as the major constituent and conservatively pick $k = 0$. The fraction of the power in the bremsstrahlung is then 0.026.

The fraction of the total energy found above the threshold for the production of that isotope can be obtained from the data of A. A. O'Dell et al.[4] They used a W-Au target, which has a much higher efficiency of bremsstrahlung production than 304L stainless steel. Hence, the values obtained by our calculation are conservative. With the total fluence, the total energy, and an estimate of the total amount of time for the irradiation, the integrated current incident on the target can be estimated. Because of the many estimates and approximations, only an order-of-magnitude integrated current can be given, but nevertheless it is very illuminating in understanding the process.

For the reactions $^{58}$Ni($\gamma$, p)$^{57}$Co, $^{55}$Mn($\gamma$, n)$^{54}$Mn, $^{60}$Ni($\gamma$, n)$^{59}$Ni, $^{52}$Cr($\gamma$, n)$^{51}$Cr, and $^{58}$Ni($\gamma$, n)$^{57}$Ni, the integral cross sections have been measured.[5–9] We have calculated the integrated electron beam on the target required to produce an activity of 20% of background (i.e., a just barely detectable activity). Tables A-2 through A-6 show the relevant quantities for three electron energies: 10, 12, and 14 MeV. The tables list the fraction of photons above threshold (from the data of ref. 4), the fraction of energy above threshold, the integral cross sections (refs. 5–9), the number of photons striking the target required to produce the activity, the energy delivered by the photons over the course of the experimental operation period, and the total energy delivered by an electron beam required to produce this photon flux. The last two lines of each table give the total ampere-seconds of runaway current to the target required for the activity and the average ampere-seconds/shot.

We have not included the other activities that could be produced by these energetic electrons because the integral cross sections are not available. If they had been available, the expected activity for a given integrated runaway current would have been higher, and the total energy delivered to produce the activity would have been even lower. Hence, inclusion of other activities would have reduced the required electron beam energy delivered to the target.

Section 5.3 mentioned a circulating current of >10 kA. This current generally occurs at the time of field ramping and has a duration of 0.1–0.4 s. For the initial ~700 shots, the current to the paddle was not measured but could have included a fraction of this circulating current. For relativistic electrons ($v \sim c$), a circulating current of 10 kA would constitute a current to a fixed target of ~440 $\mu$A. For a

Table A-2. The photoreaction $^{58}Ni(\gamma, p)^{57}Co$ by 10-, 12-, and 14-MeV electrons ($E_{th} = 8.17$ MeV)

| | $E_e$ | | |
|---|---|---|---|
| | 10 MeV | 12 MeV | 14 MeV |
| Fraction of photons $> E_{th}$ | 0.0366 | 0.0702 | 0.111 |
| Fraction of photon energy $> E_{th}$ | $9.5 \times 10^{-4}$ | $1.8 \times 10^{-3}$ | $2.9 \times 10^{-3}$ |
| $\int \sigma \cdot dE$, MeV·mb | ~0.1 | ~1 | ~7 |
| Number of photons to cause activity of 20% of background | $\sim 8 \times 10^{15}$ | $\sim 1.6 \times 10^{15}$ | $\sim 3.6 \times 10^{14}$ |
| Energy delivered by photons with $E > E_{th}$, MeV | $\sim 7.2 \times 10^{16}$ | $\sim 1.6 \times 10^{16}$ | $\sim 4 \times 10^{15}$ |
| Energy delivered by electron beam, MeV | $\sim 7.6 \times 10^{19}$ | $\sim 8.9 \times 10^{18}$ | $\sim 1.4 \times 10^{18}$ |
| $\int I \cdot dt$ for all shots, mA·s | ~1300 | ~120 | ~0.17 |
| Average $\int I \cdot dt$/shot, mA·s | ~1.8 | ~0.17 | ~0.024 |

Table A-3. The photoreaction $^{55}Mn(\gamma, n)^{54}Mn$ by 10-, 12-, and 14-MeV electrons ($E_{th}$ = 10.2 MeV)

| | $E_e$ | | |
|---|---|---|---|
| | 10 MeV | 12 MeV | 14 MeV |
| Fraction of photons > $E_{th}$ | 0 | 0.0133 | 0.359 |
| Fraction of photon energy > $E_{th}$ | 0 | $3.46 \times 10^{-3}$ | $9.33 \times 10^{-4}$ |
| $\int \sigma \cdot dE$, MeV·mb | 0 | ~10 | ~40 |
| Number of photons to cause activity of 20% of background | — | $\sim 2.8 \times 10^{14}$ | $\sim 1.4 \times 10^{14}$ |
| Energy delivered by photons with $E > E_{th}$, MeV | — | $\sim 3.1 \times 10^{15}$ | $\sim 1.7 \times 10^{15}$ |
| Energy delivered by electron beam, MeV | — | $\sim 9.0 \times 10^{17}$ | $\sim 1.9 \times 10^{18}$ |
| $\int I \cdot dt$ for all shots, mA·s | — | ~12 | ~22 |
| Average $\int I \cdot dt$/shot, $\mu$A·s | — | ~18 | ~32 |

Table A-4. The photoreaction $^{60}Ni(\gamma, n)^{59}Ni$ by 10-, 12-, and 14-MeV electrons ($E_{th}$ = 11.4 MeV)

| | $E_e$ | | |
|---|---|---|---|
| | 10 MeV | 12 MeV | 14 MeV |
| Fraction of photons > $E_{th}$ | 0 | 0.0008 | 0.0186 |
| Fraction of photon energy > $E_{th}$ | 0 | $2.08 \times 10^{-5}$ | $4.84 \times 10^{-4}$ |
| $\int \sigma \cdot dE$, MeV·mb | 0 | ~1.5 | ~26 |
| Number of photons to cause activity of 20% of background | — | $\sim 3.4 \times 10^{19}$ | $\sim 8.6 \times 10^{18}$ |
| Energy delivered by photons with $E > E_{th}$, MeV | — | $\sim 4.0 \times 10^{20}$ | $\sim 1.1 \times 10^{20}$ |
| Energy delivered by electron beam, MeV | — | $\sim 1.9 \times 10^{25}$ | $\sim 2.2 \times 10^{23}$ |
| $\int I \cdot dt$ for all shots, kA·s | — | ~268 | ~0.269 |
| Average $\int I \cdot dt$/shot, A·s | — | ~380 | ~3.8 |

Table A-5. The photoreaction $^{52}Cr(\gamma, n)^{51}Cr$ by 10-, 12-, and 14-MeV electrons ($E_{th}$ = 12.04 MeV)

| | $E_e$ | | |
|---|---|---|---|
| | 10 MeV | 12 MeV | 14 MeV |
| Fraction of photons $> E_{th}$ | 0 | 0 | 0.0117 |
| Fraction of photon energy $> E_{th}$ | 0 | 0 | $3.04 \times 10^{-4}$ |
| $\int \sigma \cdot dE$, MeV·mb | 0 | 0 | ~20 |
| Number of photons to cause activity of 20% of background | — | — | $\sim 1.6 \times 10^{12}$ |
| Energy delivered by photons with $E > E_{th}$, MeV | — | — | $\sim 2.1 \times 10^{13}$ |
| Energy delivered by electron beam, MeV | — | — | $\sim 6.9 \times 10^{16}$ |
| $\int I \cdot dt$ for all shots, mA·s | — | — | ~0.82 |
| Average $\int I \cdot dt$/shot, $\mu$A·s | — | — | ~1.1 |

Table A-6. The photoreaction $^{58}Cr(\gamma, n)^{57}Cr$ by 10-, 12-, and 14-MeV electrons ($E_{th}$ = 12.2 MeV)

| | $E_e$ | | |
|---|---|---|---|
| | 10 MeV | 12 MeV | 14 MeV |
| Fraction of photons $> E_{th}$ | 0 | 0 | 0.00857 |
| Fraction of photon energy $> E_{th}$ | 0 | 0 | $2.23 \times 10^{-4}$ |
| $\int \sigma \cdot dE$, MeV·mb | 0 | 0 | ~7 |
| Number of photons to cause activity of 20% of background | — | — | $\sim 4.7 \times 10^{11}$ |
| Energy delivered by photons with $E > E_{th}$, MeV | — | — | $\sim 6.1 \times 10^{12}$ |
| Energy delivered by electron beam, MeV | — | — | $\sim 2.8 \times 10^{16}$ |
| $\int I \cdot dt$ for all shots, mA·s | — | — | ~0.33 |
| Average $\int I \cdot dt$/shot, $\mu$A·s | — | — | ~0.47 |

typical shot, this would constitute an integrated current of ~200 $\mu$A·s. For the 12- and 14-MeV cases, this equals or exceeds the calculated values in Tables A-2 through A-6. As discussed in Sect. 5.4, the measured current to the paddle in the second phase of the experiment was more than sufficient to have produced some activity under the assumption that it was at 10, 12, or 14 MeV. We can conclude that the required electron current was readily available during the period of operation, even allowing for large errors in our estimates. Hence, we can reasonably conclude that a significant population of runaway electrons of 12 to 14 MeV does not occur in ATF.

## REFERENCES


1. C. W. Barnes, J. M. Stavely, Jr., and J. D. Strachan, *Nucl. Fusion* **21**, 1469–73 (1981).
2. S. Besshou, O. Motojima, A. Iiyoshi, and K. Uo, *J. Nucl. Sci. Technol. (Japan)* **19**, 821–30 (1982).
3. H. W. Koch and J. W. Motz, *Rev. Mod. Phys.* **31**, 920 (1959).
4. A. A. O'Dell et al., *Nucl. Instrum. Methods* **61**, 340–6 (1968).
5. B. S. Ishkhanov et al., *Sov. J. Nucl. Energy* **11**, 272–5 (1970).
6. R. A. Alvarez et al., in *Proceedings of the International Conference on Photonuclear Reactions and Applications*, Asilomar, CONF-730301, Lawrence Livermore Laboratory, p. 545 (1973).
7. B. I. Goryachev et al., *Sov. J. Nucl. Phys.* **11**, 141 (1970).
8. B. I. Goryachev et al., *Bull. Acad. Sci. U.S.S.R.–Phys. Ser.* **33**, 1588 (1969).
9. S. C. Fultz et al., in *Proceedings of the International Conference on Photonuclear Reactions and Applications*, Asilomar, CONF-730301, Lawrence Livermore Laboratory, p. 549 (1973).

ORNL/TM-10988
Dist. Category UC-420

## INTERNAL DISTRIBUTION

1–2. G. L. Bell
3. R. J. Colchin
4–5. W. R. DeVan
6. R. A. Dory
7. J. L. Dunlap
8–9. C. C. Eberle
10–14. A. C. England
15–16. R. H. Fowler
17–18. W. A. Gabbard
19–20. J. C. Glowienka
21–22. J. H. Harris
23. H. H. Haselton
24–25. G. R. Haste
26. R. C. Isler
27. T. C. Jernigan
28–26. R. R. Kindsfather
30. J. F. Lyon
31–32. R. N. Morris
33–34. M. Murakami
35–36. G. H. Neilson
37–38. D. A. Rasmussen
39–40. J. A. Rome
41–42. M. J. Saltmarsh
43. J. Sheffield
44–45. J. B. Wilgen
46–47. W. R. Wing
48–49. K. G. Young
50–51. Laboratory Records Department
52. Laboratory Records, ORNL-RC
53. Central Research Library
54. Document Reference Section
55. Fusion Energy Division Library
56–57. Fusion Energy Division Publications Office
58. ORNL Patent Office

## EXTERNAL DISTRIBUTION

59. Office of the Assistant Manager for Energy Research and Development, U.S. Department of Energy, Oak Ridge Operations Office, P. O. Box 2001, Oak Ridge, TN 37831-8705
60. J. D. Callen, Department of Nuclear Engineering, University of Wisconsin, Madison, WI 53706-1687
61. J. F. Clarke, Director, Office of Fusion Energy, Office of Energy Research, ER-50 Germantown, U.S. Department of Energy, Washington, DC 20545
62. R. W. Conn, Department of Chemical, Nuclear, and Thermal Engineering, University of California, Los Angeles, CA 90024
63. S. O. Dean, Fusion Power Associates, Inc., 2 Professional Drive, Suite 248, Gaithersburg, MD 20879
64. H. K. Forsen, Bechtel Group, Inc., Research Engineering, P. O. Box 3965, San Francisco, CA 94119
65. J. R. Gilleland, L-644, Lawrence Livermore National Laboratory, P.O. Box 5511, Livermore, CA 94550

66. R. W. Gould, Department of Applied Physics, California Institute of Technology, Pasadena, CA 91125
67. R. A. Gross, Plasma Research Laboratory, Columbia University, New York, NY 10027
68. D. M. Meade, Princeton Plasma Physics Laboratory, P.O. Box 451, Princeton, NJ 08543
69. M. Roberts, International Programs, Office of Fusion Energy, Office of Energy Research, ER-52 Germantown, U.S. Department of Energy, Washington, DC 20545
70. W. M. Stacey, School of Nuclear Engineering and Health Physics, Georgia Institute of Technology, Atlanta, GA 30332
71. D. Steiner, Nuclear Engineering Department, NES Building, Tibbetts Avenue, Rensselaer Polytechnic Institute, Troy, NY 12181
72. R. Varma, Physical Research Laboratory, Navrangpura, Ahmedabad 380009, India
73. Bibliothek, Max-Planck Institut für Plasmaphysik, Boltzmannstrasse 2, D-8046 Garching, Federal Republic of Germany
74. Bibliothek, Institut für Plasmaphysik, KFA Jülich GmbH, Postfach 1913, D-5170 Jülich, Federal Republic of Germany
75. Bibliothek, KfK Karlsruhe GmbH, Postfach 3640, D-7500 Karlsruhe 1, Federal Republic of Germany
76. Bibliotheque, Centre de Recherches en Physique des Plasmas, Ecole Polytechnique Fédérale de Lausanne, 21 Avenue des Bains, CH-1007 Lausanne, Switzerland
77. R. Aymar, CEN/Cadarache, Departement de Recherches sur la Fusion Contrôlée, F-13108 Saint-Paul-lez-Durance Cedex, France
78. Bibliothèque, CEN/Cadarache, F-13108 Saint-Paul-lez-Durance Cedex, France
79. Library, Culham Laboratory, UKAEA, Abingdon, Oxfordshire, OX14 3DB, England
80. Library, JET Joint Undertaking, Abingdon, Oxfordshire OX14 3EA, England
81. Library, FOM-Instituut voor Plasmafysica, Rijnhuizen, Edisonbaan 14, 3439 MN Nieuwegein, The Netherlands
82. Library, Institute of Plasma Physics, Nagoya University, Chikusa-ku, Nagoya 464, Japan
83. Library, International Centre for Theoretical Physics, P.O. Box 586, I-34100 Trieste, Italy
84. Library, Centro Richerche Energia Frascati, C.P. 65, I-00044 Frascati (Roma), Italy
85. Library, Plasma Physics Laboratory, Kyoto University, Gokasho, Uji, Kyoto 611, Japan
86. Plasma Research Laboratory, Australian National University, P.O. Box 4, Canberra, A.C.T. 2601, Australia

87. Library, Japan Atomic Energy Research Institute, Naka Fusion Research Establishment, 801-1 Mukoyama, Naka-machi, Naka-gun, Ibaraki-ken, Japan
88. G. A. Eliseev, I. V. Kurchatov Institute of Atomic Energy, P. O. Box 3402, 123182 Moscow, U.S.S.R.
89. V. A. Glukhikh, Scientific-Research Institute of Electro-Physical Apparatus, 188631 Leningrad, U.S.S.R.
90. I. Shpigel, Institute of General Physics, U.S.S.R. Academy of Sciences, Ulitsa Vavilova 38, Moscow, U.S.S.R.
91. D. D. Ryutov, Institute of Nuclear Physics, Siberian Branch of the Academy of Sciences of the U.S.S.R., Sovetskaya St. 5, 630090 Novosibirsk, U.S.S.R.
92. V. T. Tolok, Kharkov Physical-Technical Institute, Academical St. 1, 310108 Kharkov, U.S.S.R.
93. Deputy Director, Southwestern Institute of Physics, P.O. Box 15, Leshan, Sichuan, China (PRC)
94. Director, The Institute of Plasma Physics, P.O. Box 26, Hefei, Anhui, China (PRC)
95. R. A. Blanken, Experimental Plasma Research Branch, Division of Applied Plasma Physics, Office of Fusion Energy, Office of Energy Research, ER-542, Germantown, U.S. Department of Energy, Washington, DC 20545
96. R. A. E. Bolton, IREQ Hydro-Quebec Research Institute, 1800 Montee Ste.-Julie, Varennes, P.Q. JOL 2P0, Canada
97. D. H. Crandall, Experimental Plasma Research Branch, Division of Applied Plasma Physics, Office of Fusion Energy, Office of Energy Research, ER-542, Germantown, U.S. Department of Energy, Washington, DC 20545
98. R. L. Freeman, General Atomics, P.O. Box 85608, San Diego, CA 92138-5608
99. K. W. Gentle, RLM 11.222, Institute for Fusion Studies, University of Texas, Austin, TX 78712
100. R. J. Goldston, Princeton Plasma Physics Laboratory, P.O. Box 451, Princeton, NJ 08543
101. J. C. Hosea, Princeton Plasma Physics Laboratory, P.O. Box 451, Princeton, NJ 08543
102. D. Markevich, Division of Confinement Systems, Office of Fusion Energy, Office of Energy Research, ER-55, Germantown, U.S. Department of Energy, Washington, DC 20545
103. R. H. McKnight, Experimental Plasma Research Branch, Division of Applied Plasma Physics, Office of Fusion Energy, Office of Energy Research, ER-542, Germantown, U.S. Department of Energy, Washington, DC 20545
104. E. Oktay, Division of Confinement Systems, Office of Fusion Energy, Office of Energy Research, ER-55, Germantown, U.S. Department of Energy, Washington, DC 20545
105. D. Overskei, General Atomics, P.O. Box 85608, San Diego, CA 92138-5608
106. R. R. Parker, Plasma Fusion Center, NW 16-288, Massachusetts Institute of Technology, Cambridge, MA 02139

107. W. L. Sadowski, Fusion Theory and Computer Services Branch, Division of Applied Plasma Physics, Office of Fusion Energy, Office of Energy Research, ER-541 Germantown, U.S. Department of Energy, Washington, DC 20545
108. J. W. Willis, Division of Confinement Systems, Office of Fusion Energy, Office of Energy Research, ER-55 Germantown, U.S. Department of Energy, Washington, DC 20545
109. A. P. Navarro, Division de Fusion, CIEMAT, Avenida Complutense 22, E-28040 Madrid, Spain
110. Laboratory for Plasma and Fusion Studies, Department of Nuclear Engineering, Seoul National University, Shinrim-dong, Gwanak-ku, Seoul 151, Korea
111. J. L. Johnson, Princeton Plasma Physics Laboratory, P.O. Box 451, Princeton, NJ 08543
112. L. M. Kovrizhnykh, Institute of General Physics, U.S.S.R. Academy of Sciences, Ulitsa Vavilova 38, 117924 Moscow, U.S.S.R.
113. O. Motojima, Plasma Physics Laboratory, Kyoto University, Gokasho, Uji, Kyoto, Japan
114. V. D. Shafranov, I. V. Kurchatov Institute of Atomic Energy, P.O. Box 3402, 123182 Moscow, U.S.S.R.
115. J. L. Shohet, Torsatron/Stellarator Laboratory, University of Wisconsin, Madison, WI 53706
116. H. Wobig, Max-Planck Institut für Plasmaphysik, D-8046 Garching, Federal Republic of Germany
117. C. W. Barnes, Princeton Plasma Physics Laboratory, P.O. Box 451, Princeton, NJ 08543
118. S. Besshou, Plasma Physics Laboratory, Kyoto University, Gokasho, Uji, Kyoto, Japan
119. S. M. Hamberger, Plasma Research Laboratory, Australian National University, P.O. Box 4, Canberra, A.C.T. 2601, Australia
120. H. Kaneko, Plasma Physics Laboratory, Kyoto University, Gokasho, Uji, Kyoto, Japan
121. H. Knöpfel, Centro Richerche Energia Frascati, C.P. 65, I-00044 Frascati (Roma), Italy
122. S. Morimoto, Plasma Physics Laboratory, Kyoto University, Gokasho, Uji, Kyoto, Japan
123. S. Okamura, Institute of Plasma Physics, Nagoya University, Chikusa-ku, Nagoya 464, Japan
124. N. Perepelkin, Kharkov Physical-Technical Institute, Academical St. 1, 310108 Kharkov, U.S.S.R.
125–161. Given distribution as shown in OSTI-4500, Energy Research (Category Distribution UC-420, Magnetic Fusion Energy)